UNIVERSIDAD DE CHILE
FACULTAD DE CIENCIAS FÍSICAS Y MATEMÁTICAS
DEPARTAMENTO DE FÍSICA

# CHARACTERIZATION OF MAGNETO-BIOCONVECTION PATTERNS IN DENSE SUSPENSIONS OF *MAGNETOSPIRILLUM GRYPHISWALDENSE*

TESIS PARA OPTAR AL GRADO DE MAGÍSTER EN CIENCIAS, MENCIÓN FÍSICA

BENJAMÍN OLIVA DESTEFANI

PROFESORA GUÍA:
María Luisa Cordero Garayar

MIEMBROS DE LA COMISIÓN:
Marcel Clerc Gavilán
Fernán Federici Noe
Francisca Guzmán Lastra

Este trabajo ha sido parcialmente financiado por:
ANID, a través de los proyectos Fondecyt 1210634 y Núcleo Milenio Física de la Materia Activa

SANTIAGO DE CHILE
2023

# CARACTERIZACIÓN DE PATRONES DE MAGNETOBIOCONVECCIÓN EN SUSPENSIONES DENSAS DE *MAGNETOSPIRILLUM GRYPHISWALDENSE*

*Magnetospirillum gryphiswaldense* es una especie de bacteria anfítrica, micro-aerofílica y magnetotáctica. Produce un organelo llamado magnetosoma, que consiste en una cadena de nanocristales de magnetita, el cual le otorga un momento dipolar magnético permanente. Gracias a eso, sus células se alinean de manera pasiva con campos magnéticos externos, lo cual se cree que les ayuda a alcanzar condiciones favorables en la naturaleza. Bajo confinamiento entre dos paredes paralelas y en presencia de un campo magnético externo perpendicular a las paredes, suspensiones densas de esta bacteria realizan un tipo de movimiento colectivo llamado magnetobioconvección, similar a los flujos de convección. En esta tesis, exploramos el comportamiento tridimensional de la magnetobioconvección, dando una descripción cualitativa del fenómeno, junto a un análisis cuantitativo de los tiempos y longitudes características de los patrones de los flujos.

Para formar los patrones, se cultivaron y concentraron suspensiones de *M. gryphiswaldense* de acuerdo a protocolos existentes. Esto implicó preparar el medio de cultivo, desplazar el oxígeno de los tubos de cultivo y centrifugar para generar suspensiones densas. La suspensión resultante fue depositada dentro de una de dos tipos de microcavidades y cubierta con un vidrio cubre objetos. Las dos microcavidades se diferencian en que una está hecha de vidrio, impidiendo la entrada de oxígeno en la cavidad, mientras que la otra esta hecha de un polímero permeable a los gases, por lo tanto, permitiendo la oxigenación. Para generar campos magnéticos homogéneos en la muestra, se fabricaron bobinas de Helmholtz las cuales fueron montadas en un microscopio, que se usó para observar y grabar la dinámica de los patrones de magnetobioconvección.

Después de un estado transitorio, el sistema alcanza un estado cuasi-estacionario, caracterizado por la formación de una variedad de patrones, de diferentes tamaños y formas, trazados por inhomogeneidades de densidad en la suspensión. Dada su forma, los patrones fueron clasificados cualitativamente en clusters, que corresponden a islas de alta densidad; celdas, caracterizadas por la presencia de estructuras geométricas alrededor de las islas de alta densidad; y bandas, que aparecen cuando flujos externos no controlados estiran los patrones mientras se forman. Cuantitativamente, tiempos y longitudes características fueron calculadas a partir de los videos grabados, y su dependencia con los parámetros experimentales, altura de confinamiento $h$, oxigenación, densidad de bacterias e intensidad del campo magnético $B_z$ fue observada. Aparte de $h$, el cual mostró determinar de manera lineal el tamaño y la separación entre las estructuras, se observó una alta cantidad de dispersión, sugiriendo la presencia de un parámetro inexplorado, como la velocidad promedio de las bacterias, el cual podría afectar fuertemente la dinámica de los patrones. Se sugirieron experimentos a realizar en el futuro con tal de explorar la influencia de otros parámetros.

## CHARACTERIZATION OF MAGNETO-BIOCONVECTION PATTERNS IN DENSE SUSPENSIONS OF *MAGNETOSPIRILLUM GRYPHISWALDENSE*

*Magnetospirillum gryphiswaldense* is a species of amphitrichous, microaerophilic magnetotactic bacteria (MTB). It produces an organelle called magnetosome consisting of a chain of magnetite nano-crystals, which endows it with a permanent magnetic dipole moment. Thanks to that, *M. gryphiswaldense* cells passively align with external magnetic fields, which is believed to help them reaching favorable conditions in water sediments in nature. Under confinement between two parallel walls and in the presence of an external magnetic field perpendicular to the walls, dense suspensions of these bacteria perform a type of collective motion called magneto-bioconvection, resembling convection flows. In this thesis, we explored the three-dimensional behavior of magneto-bioconvection, providing a qualitative description of the phenomenon, together with quantitative analysis of the characteristic temporal and length scales of the flow pattern.

In order to accomplish pattern formation in MTB suspensions, cultures of *M. gryphiswaldense* were grown and densified in accordance with existing protocols. This involved preparing the culture medium, displacing oxygen out of the culture tubes and centrifugating them to generate a dense suspension of bacteria. The resulting suspension was then deposited inside one of two types of micro-cavities, and covered with a glass slide. The two micro-cavities differ in their material: one of them is made of glass, which prevents the inflow of Oxygen, while the other one is made from a polymer, which is permeate to gasses and thus allows oxygenation of the bacterial suspension. To generate homogeneous magnetic fields in the sample, Helmholtz coils were fabricated and mounted in a microscope, which is then used to observe and record the dynamics of the magneto-bioconvection pattern.

After a transient state, the system reached a quasi-stationary state, characterized by the formation of a variety of patterns of different sizes and shapes, drawn by density inhomogeneities within the suspension. According to their form, the patterns were qualitatively classified into clusters, which are isolated high density islands; cells, characterized by the presence of geometrical structures surrounding the high density islands; and bands, that appeared when uncontrolled external flows stretched the patterns as they formed. Quantitatively, characteristic times and lengths were computed from the recorded videos and their dependence on the experimental parameters, confinement height $h$, the oxygenation, the density of bacteria and the magnetic field intensity $B_z$ was observed. Aside of $h$, which showed to linearly determine the structures size and separation, a lot of dispersion was observed, suggesting the presence of an unexplored parameter, such as the average bacteria speed, that could strongly affect the pattern dynamics. Future experiments were suggested in order to explore the influence of other parameters.

*"Por ende, el tema no es si es que logramos el Anarquismo*
*hoy, mañana, o en diez siglos más,*
*sino que caminemos hacia el Anarquismo,*
*hoy, mañana y siempre."*

*-Errico Malatesta*

# Agradecimientos

Quisiera agradecer en primera instancia y de manera muy general, a todas las personas que me he topado a lo largo del trabajo de mi tesis, y que de manera directa o indirecta han sido un aporte para mi desarrollo como persona. En particular, quiero agradecer a mi madre y padre, quienes han sido siempre un apoyo incondicional pero, a su vez, una fuente de honestidad. Quiero agradecer a mi hermana Montserrat, por su preocupación y liviandad. A mis amigas de la vida, Alejandra, Pamela y Rode por su compañía en los momentos mas difíciles. A Farid, Erick y Alolo. Es dificil poner en palabras lo significativos que han sido para mí en esta etapa. A mi amigo Ignacio, terminamos el pregrado y comenzamos el magíster juntos. Una compañía esencial por parte de la persona que me mostró que era posible graduarse. A Francisco y Ambar, quienes me acogieron como parte de su familia. A Jose y Javi, por la calida compañía en el tiempo que hemos vivido juntos. A Nicolas, quien junto a Ignacio empujaron mis límites jugando SSBM. A Gabriel, un muy buen apoyo en el proceso que vivimos juntos. A la gente del tercero: Claudia, Lucas, Gerd, Colipi y Paloma. A Cristian, quien se convirtió en el amigo que necesité en París. A Guillermo, quien se convirtió en una muy buena y necesaria compañía al momento de hacer experimentos. A Edgardo, Juan Pablo, Aguayo, Fernanda, Pablo, Paulo y Kevin. Excelentes colegas, quienes siempre aportaron con comentarios e introspecciones respecto a mi trabajo. De más está decir las instancias de distensión. Balístico a tiempos cortos, difusivo a tiempos largos, de eso se trata la vida. A Manuel, un compañero Anarquista del otro lado del Atlántico. A Gabriel Ramos, quien se convirtió en un referente al enseñarme los protocolos de cultivo de las bacterias magnetotácticas. A Pamela y Oscar, por interesarse en la investigación que hemos iniciado y por su disposición a conocer el trabajo experimental. A la profesora María Luisa, por confiar en mí y permitirme explorar un fenómeno que en un principio no estaba considerado en los planes de investigación. Finalmente, a todas y todos los integrantes del Núcleo Milenio Física de la Materia Activa, quienes siempre me hicieron sentir que tenía algo bueno que aportar a la ciencia.

# TABLE OF CONTENT

# Table index

# Figure Index

# Chapter 1

# Introduction

## 1.1. Active Matter

Active Matter are condensed systems, composed of a group of particles in which each unit has its own motor, allowing them to extract energy from the environment to generate movement. Because of this, active matter systems are out of equilibrium. If the elements that compose active systems are allowed to interact between themselves, it is not difficult to note the emergence of collective behavior (figure 1.1). This depends on the parameters related to the interaction [Vicsek et al., 1995, Vicsek and Zafeiris, 2012, Chaté et al., 2008, Chaté and Mahault, 2019] and depending on that, is the type of collective motion that can arise. Good examples of this can be found in, but are not restricted to, groups of living organisms [Camazine et al., 2001], such as bird and sheep flocks [Cavagna et al., 2010, Arnold and Pahl, 1974], fish schools [Lopez et al., 2012], human groups [Kok et al., 2016], ant colonies [Gordon, 2019], cells in tissues [Trepat et al., 2009] and bacterial systems [Czirók et al., 2001, Ng and Bassler, 2009], to name a few. Some non-living examples of active matter can be found in active colloids [Aranson, 2013] or in the standard motility assay [Sumino et al., 2012, Schaller et al., 2010].

Between the broad variety of systems that can be considered as active, microswimmers, such as bacteria, unicellular algae or ciliate protozoa, have the advantage of being easily studied in a laboratory [Zhang et al., 2010]. In the next section, we will explore the physics of microswimmers, to understand how a specific type of collective motion can emerge.

### 1.1.1. Microswimmers: Hydrodynamics

How can microswimmers move through a fluid is, surprisingly, not a trivial problem. To answer that, we need first to build some intuition regarding the forces that are present. Let us introduce the dimensionless quantity known as the Reynolds number, defined as the ratio of inertial forces to viscous forces [Purcell, 1977],

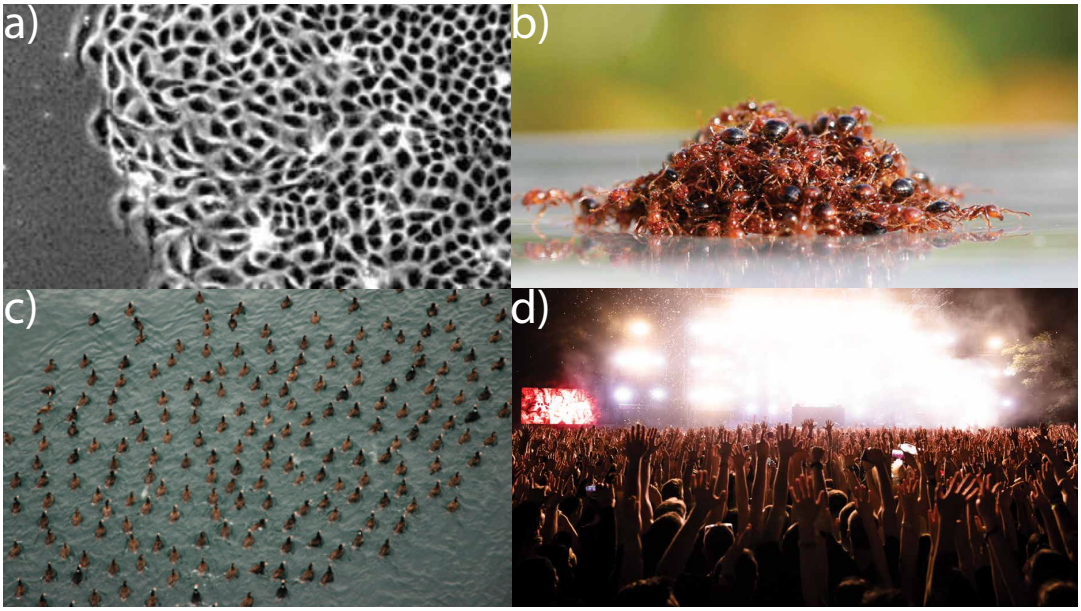


Figure 1.1: a) Collective motion in advancing Madin-Derby canine kidney epithelial cells, where each cell engages in a tug-of-war that integrates local force generation into a global state of tensile stress [Trepat et al., 2009]. b) Fire ants self-assembling into rafts in order to survive to floods [Mlot et al., 2011]. c) Flocks of surf scoters (*Melanitta perspicillata*) exhibit a high degree of cohesion, polarization, well-defined spacing structure and synchrony in dives [Lukeman et al., 2010]. d) When exposed to the right stimulus, dense group of humans are able to present coherent orientations, performing synchronized vertical and horizontal movement and sound (freepik.es).

$$Re = \frac{\text{inertial forces}}{\text{viscous forces}} = \frac{dv\rho}{\eta}, \tag{1.1}$$

where $d$ is the characteristic size and $v$ the typical speed of the swimmer, $\rho$ is the fluid's density and $\eta$ is the fluid viscosity. For water, $\eta = 1 \times 10^{-3}\,\mathrm{Pa\,s}$ and $\rho = 1 \times 10^{3}\,\mathrm{kg\,m^{-3}}$. Different swimmers, in different scales, will have different Reynolds numbers. For example, a person ($d \sim 1\,\mathrm{m}$) swimming in water ($v \sim 1\,\mathrm{m\,s^{-1}}$) will be characterized by a Reynolds number of $\sim 10^6$. For a goldfish ($d \sim 1 \times 10^{-1}\,\mathrm{m}$ and $v \sim 0.5\,\mathrm{m\,s^{-1}}$) it might be $\sim 5 \times 10^4$. As for microorganisms ($d \sim 10 \times 10^{-6}\,\mathrm{m}$ and $v \sim 10 \times 10^{-6}\,\mathrm{m\,s^{-1}}$), it is $\sim 10^{-4}$. For the latter case, inertial forces are completely negligible in comparison with viscous forces.

A swimmer must generate movement inside a fluid via cyclical deformations of its body to swim. A simple and basic example of deformation to generate movement at $Re \sim 10^2$ is the scallop, a bivalve mollusc consisting of two shells jointed together by an elastic hinge. It has one degree of freedom to deform its body, one axis around which it can open or close the shells. When performed cyclically, this motion provokes the propulsion of the scallop, strongly depending on inertia to keep moving. If this motion is performed at $Re \ll 1$, the scallop would not be able to displace. Because of the high predominance of viscosity over

inertia, when closing the shells, it will displace a distance in one direction, but when opening the shells, it will move the same distance in the opposite direction, as shown in figure 1.2.

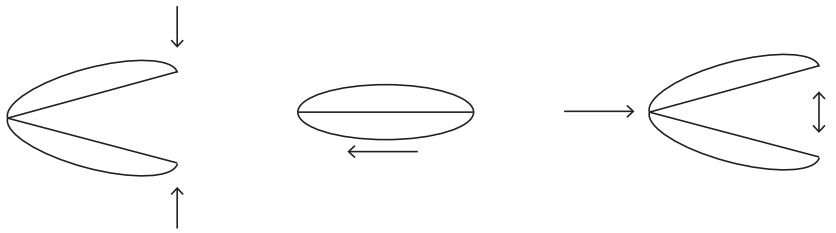

Figure 1.2: Diagram showing the impossibility of a scallop to move if it were to swim at low Reynolds number. One deformation performed in one direction will generate a movement that will be countered by the same deformation performed in the opposite direction, leading to a net displacement of zero.

But not everything is lost. The main reason why this swimming strategy is not good at low Reynolds number, is because the Stokes equation, that governs fluid motion at low $Re$, given by

$$\nabla p = \eta \nabla^2 \mathbf{v}, \tag{1.2}$$

where $p$ is the pressure field and $\mathbf{v}$ is the velocity field, is linear and time independent, meaning that it is not possible to distinguish between forward and backward in a reciprocal motion. This leads to the condition of motion at low Reynolds number: the microswimmer should perform a cyclical but not reciprocal motion in order to displace. In other words, the cyclical deformation cannot be the same movement performed in one direction and then reversed in the other direction. For example, the "breaststroke", performed by unicellular alga *Chlamydomonas Nivalis*, is a strategy of swimming that is a non-reciprocal cyclical motion. Another type of movement that meets the requirements is a wave-like type of deformation. Some bacteria, such as *Magnetospirillum gryphiswaldense*, rotate one or more helical flagella thanks to rotary motors embedded in the cell wall. Spermatozoa, a singly flagellated eukaryote, swims by traveling waves in their flagellum, through internal sliding of polymeric filaments driven by molecular motors [Lauga, 2011].

A question that arises from the movement of swimming microorganisms is: How does a microswimmer affect the flow field around it? In order to understand the flow of the collective motion, it is important to have a deeper understanding of their individual behavior.

The Stokeslet (figure 1.3a)) is the solution to the flow field due to a point force in a low Reynolds number regime [Hancock, 1953]. The flow decays as $1/r$, where $r$ is the distance to the location of the point force. By differentiating the expression of the Stokeslet with respect to $r$, it is possible to obtain a complete set of singularities [Lauga and Powers, 2009], such as the force dipole, decaying as $1/r^2$ (figure 1.3b) or the source dipole (doublet) and force

quadrupoles (figure 1.3c), decaying as $1/r^3$ [Chwang and Wu, 1975]. Since equation (1.2) is linear, it can be solved by linear superposition of the mentioned singularities. If one wants to find the flow field generated by a 3D body, it is possible to distribute, for example, Stokeslets or doublets inside the body in a way that the solution meets the boundary conditions on the body surface. For example, the flow field around a self-propelled spherical body can be computed by a combination of a Stokeslet and a doublet.

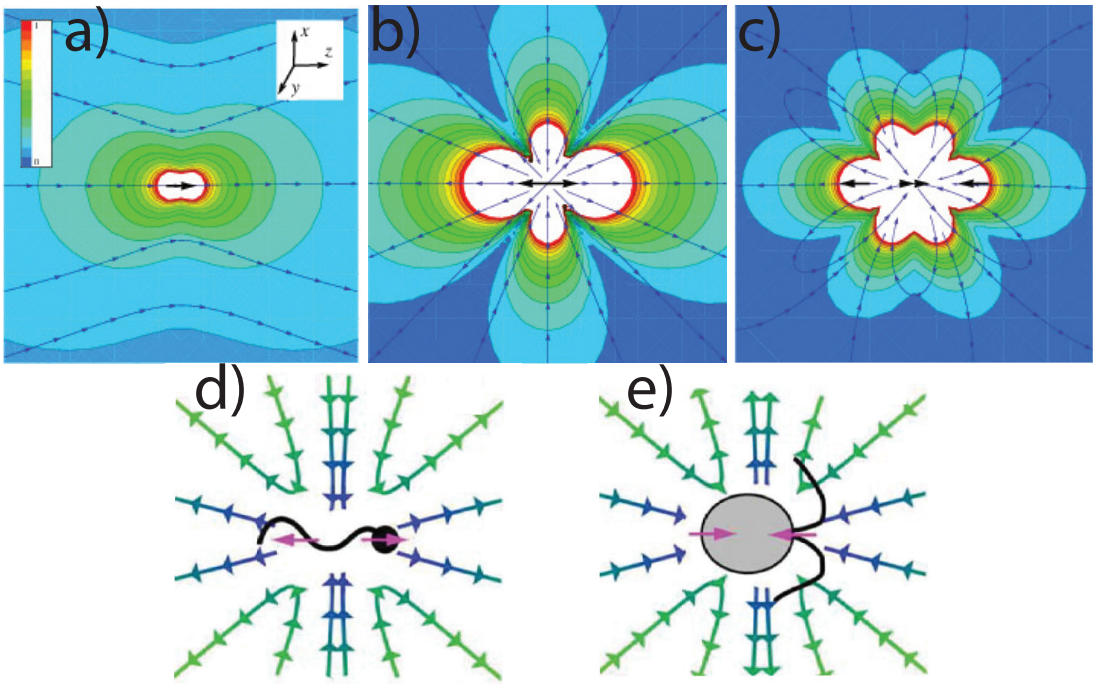


Figure 1.3: Flow fields produced by a micro-swimmer corresponding to different multipole expansion singularities from the laboratory frame. a) Stokeslet. b) Dipole of forces. c) Quadrupole of forces. d) Schematic of the flow field of pusher-type micro-swimmer *E. coli*. e) Schematic of the flow field of puller-type micro-swimmer *Chlaymdomonas*. Diagrams taken from [Mathijssen, 2016].

As for micro-swimmers, many of them have, to a good approximation, a shape that is cylindrically symmetric about the swimming direction. This restricts the number of non-zero components of the swimmer multipole moments. Also, since microswimmers move in a flow at low Reynolds numbers, the description should be force-free and torque-free in the far-field description. In consequence, the swimming cell is well represented, in general, by a symmetric force dipole (figure 1.3b)), that can be seen as two forces, the drag and the propulsion, pointing in opposite directions [Mathijssen, 2016]. One important consequence of this is that two types of flows can arise, being strictly related to the swimming strategy of the microswimmer. In one case, the forces point away from each other, leading the cell to push fluid from the front and the rear, and to pull fluid from the sides. This is called an extensile flow and the type of swimmers are called "pushers" (figure 1.3 d)). The second case corresponds to the inverse behavior. The forces point towards each other, leading the cell to pull fluid from the

front and the rear and to push fluid from the sides. This is called a contractile flow, and the swimmers are called "pullers" (figure 1.3 e)). Which strategy will a microswimmer perform, has important consequences in the type of collective behavior they can display, as will be seen in sections 1.3.2 and 1.3.3.

### 1.1.2. Microswimmers: Taxis

Besides generating the displacement of the cell, the swimming strategy of microorganisms also has to allow changes in the direction of propulsion in order to lead the organism to favorable environments. The bacterium *Escherichia coli*, shown in figure 1.4a), swims thanks to the presence of various flagella that rotate together counterclockwise (CCW), forming a bundle that directs the cell forward in a straight line, in what is called a "run". Spontaneously, some flagella start to rotate clockwise (CW), disrupting the bundle and generating a switch in the direction of motion, or "tumble", as diagrammed in figure e1.4b). The cell then returns to swim in a new direction. This cycle of moves helps *E. coli* to sense gradients of stimuli in the environment and to change the duration of the "runs" and the frequency of the "tumbles" (figure 1.4c-d), biasing the randomness of the swimming pattern up gradients of chemo-attractants [Armitage, 2001, Berg, 2004].

Unicellular algae of the *Chlamydomonas* genus swim thanks to two flagella located at the front of the cell (figure 1.5a-b), that perform a breaststroke-style type of motion. Unlike *E. coli*, *Chlamydomonas* do not swim in straight lines, but rather in a helical path, due to a CCW rotation of its body around the longitudinal axis. As the cell rotates, if light hits the cell perpendicular to the longitudinal axis of the body, an intermittent signal is generated as the eyespot, a light-sensing organelle, points towards or away from the light source, working as an antenna [Foster and Smyth, 1980]. This generates changes in the concentration of calcium ions inside the flagella, alternating the beating patterns of the cis and trans flagella (named after their position relative to the eyespot), producing an overall reorientation of the cell, as shown in figure 1.5c), until its longitudinal axis points towards the light source [Kamiya and Witman, 1984].

The two phenomena explained above are called chemotaxis and phototaxis respectively. Both rely on an internal mechanism integrated in the cell to guide it towards favorable or away from unfavorable environmental conditions. There exist other types of taxes, such as gravitaxis, gyrotaxis or magnetotaxis, which are passive types of biases induced in the cell swimming direction due to external torques from gravitational, hydrodynamic or magnetic interactions, respectively. These types of taxes will be explained in more detail in sections 1.3 and 1.1.3.

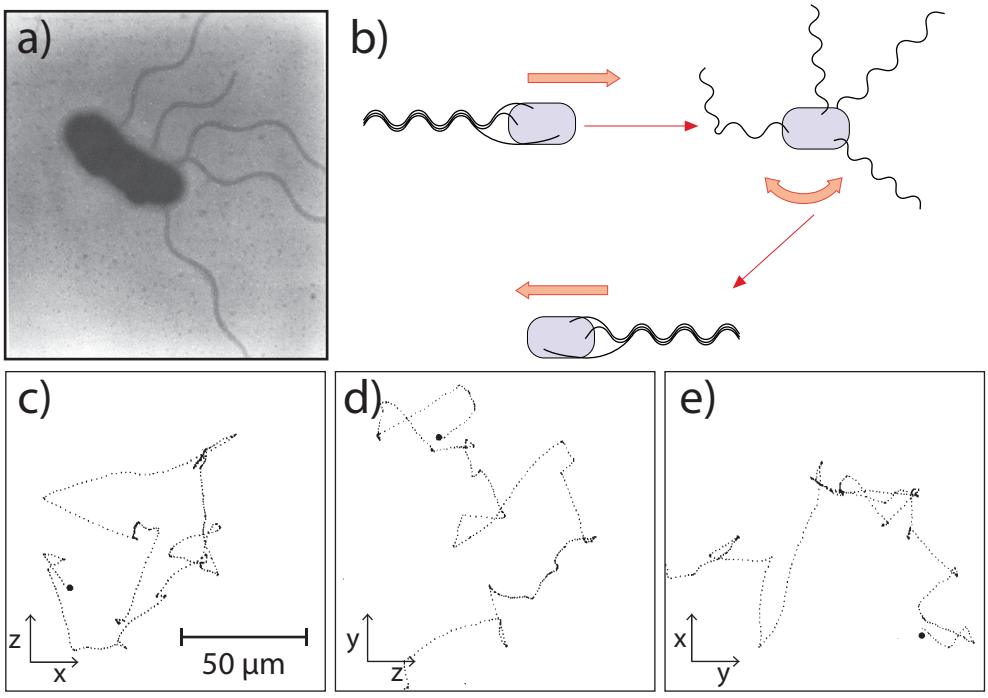


Figure 1.4: *E. coli* senses the environment as it performs a random walk through run and tumble cycles. a) Electron micrograph of *E. coli*. For scale, the diameter of the cell body is about 1 µm. Image taken from [Berg, 2004]. b) Diagram showing the run and tumble process, as the flagellar bundle is disrupted and then reassembled. Figure adapted from [Armitage, 2001]. c-e) Planar projections of an *E. coli* trajectory in different planes. The time difference between tumbles isn't constant, generating different run lengths. Figures extracted from [Berg and Brown, 1972].

### 1.1.3. Magnetotactic Bacteria

Discovered in 1975 by Richard Blakemore [Blakemore, 1975] in a sample taken from Cape Cod, Massachusetts (northern hemisphere), magnetotactic bacteria (MTB) are unicellular organisms that present a type of guidance imposed by external magnetic fields. This type of interaction was called magnetotaxis. The first type of MTB showed a tendency to swim parallel to external magnetic field lines, but in a second work, Blakemore reported that MTB coming from Christchurch, New Zealand, in the southern hemisphere, express the opposite behavior, meaning, they had a tendency to swim anti-parallel to the external magnetic field lines [Blakemore et al., 1980]. Those observations lead to the classification of MTB into two types, the north-seekers (NS) and the south-seekers (SS).

Magnetotaxis is possible thanks to the presence of a biomineralized organelle, called magnetosome (figure 1.6), consisting in a chain of magnetic mineral crystals of magnetite ($Fe_3O_4$) or greigite ($Fe_3S_4$). Each individual crystal can range from 35 to 120 nm in size, locating the crystals within the range of single-magnetic-domain, therefore, having the highest possible magnetic moment per unit volume [Lefèvre and Bazylinski, 2013].

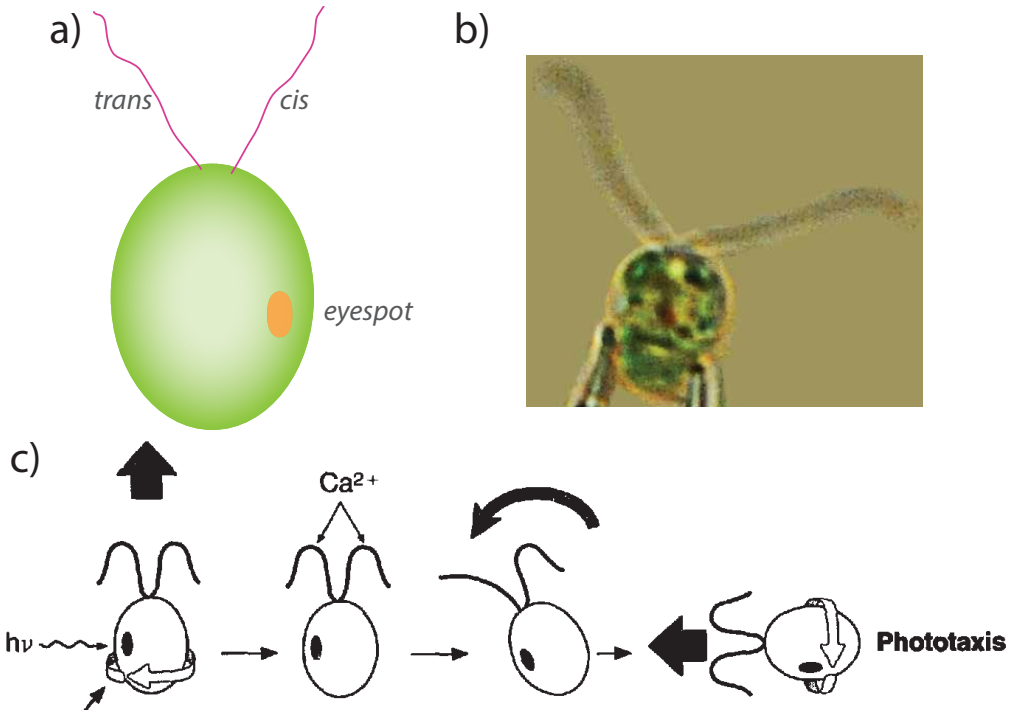


Figure 1.5: Unicellular algae of the *Chlamydomonas* genus are able to perform phototaxis. a) Diagram of the shape of a *Chlamydomonas reinhardtii*, showing the location of the eyespot and the two flagella, differentiated as cis and trans. b) Photograph of a *Chlamydomonas reinhardtii* cell. For scale, the cell has a diameter of ∼10 µm. c) Diagram showing the reorientation process of a *Chlamydomonas* cell. The cis and trans flagella respond different to calcium concentration variations, that occur whenever light hits the eyespot intermittently. This alters the beating patter of the flagella, generating a reorientation of the cell. a) and b) were taken from [Goldstein, 2015]. c) was extracted from [Witman, 1993].

Besides magnetotaxis, magnetotactic bacteria also have aerotaxis [Bazylinski and Frankel, 2004], which is a specific type of chemotaxis where the cell responds to oxygen gradients. MTB prefer zones with low oxygen concentrations, so they are said to be anaerobic or microaerophilic. This behavior, together with magnetotaxis, acts as a guide, reducing a three dimensional sensing problem to one dimension, leading to the use of magneto-aerotaxis (or magnetic guided aerotaxis) as the correct term for describing the tactic behavior of MTB.

The species of magnetotactic bacteria that was used for the experiments in this thesis is *Magnetospirillum gryphiswaldense* (figure 1.6), strain MSR-1 [Schleifer et al., 1991], a helical shaped species of MTB that propels thanks to the presence of two flagella located at each end of its body. Bacteria from the *magnetospirillum* genus are axially symmetric, and their swimming polarity can switch relative to the magnetic polarity, meaning that sometimes one cell can swim towards one magnetic pole but spontaneously switch its direction towards the other pole, performing a reversal, changing from NS to SS or vice versa. In a previous work

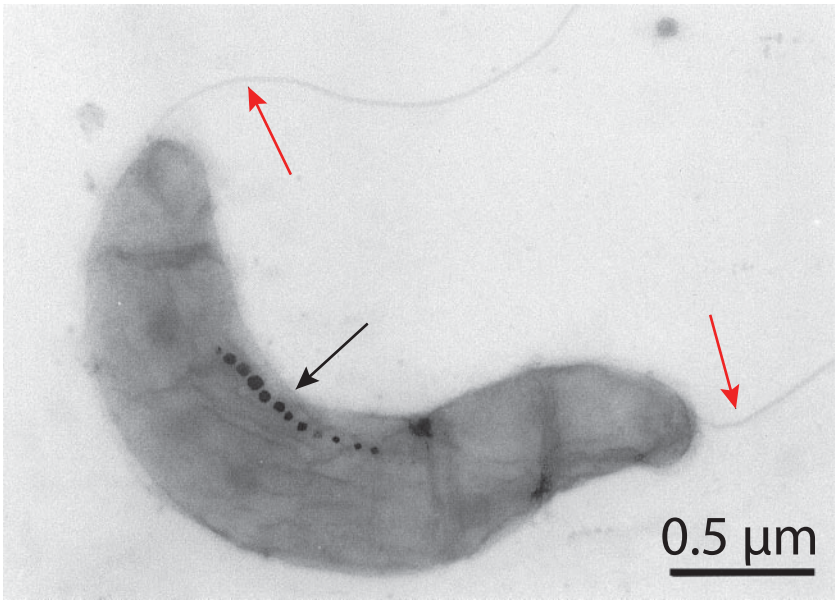


Figure 1.6: Electron micrograph of *Magnetospirillum gryphiswaldense*. The black arrow indicates the magnetosome inside the cell. The red arrows point at the two polar flagella. The helical shape of the body, characteristic of the *Magnetospirillum* genus is visible. Image extracted from [Schüler and Frankel, 1999].

on *Magnetorspirillum magneticum*, Murat et al. showed that this run and reversal events are a consequence of the coordinated rotation of the two pollar flagella [Murat et al., 2015]. Sometimes, the coordination was lost, leading the cell to stop swimming. It was proposed that the times of run, reversal and pauses was highly controlled by oxygen concentrations based on another work, where it was suggested that aerotaxis is the dominant tactic behavior [Popp et al., 2014]. For the moment, no studies have explored the movement statistics of bacteria from the *magnetospirillum* genus under oxygen gradients. Nevertheless, we observed that, in general, there exists a predominant persistence towards one swimming polarity, since the switching in the direction usually persists for small windows of time. This can be observed in figure 1.7, where a diluted suspension of MTB inside a cavity, trapped between two glass slides and affected by an external magnetic field, shows the separation of the population in two groups: those swimming towards the magnetic south pole (1.7a)) and those swimming towards the magnetic north pole (1.7b)).

## 1.2. Motivation

When learning the protocols to cultivate and densify MTB, an exploratory experiment was performed. A drop of a dense suspension of MTB with a volume of $\sim 10\,\mu L$ was placed on a glass slide and observed under the microscope. While observing, a ring-shaped magnet was placed around the drop, as shown in figure 1.8.

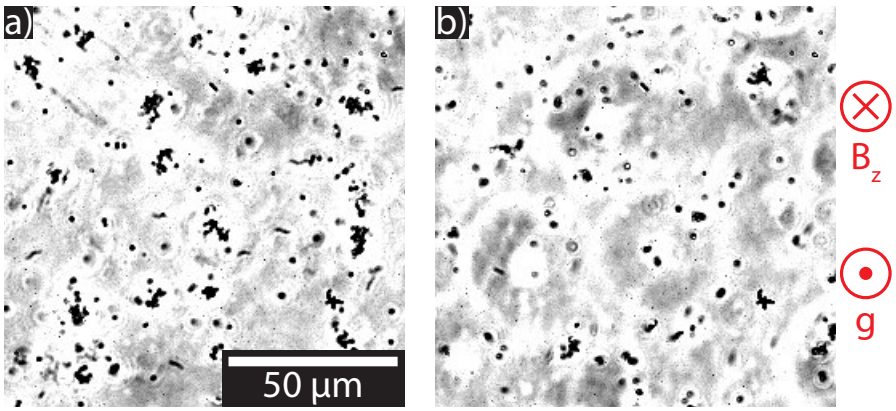


Figure 1.7: Snapshots of a diluted suspension of bacteria, confined between two glass slides. In both cases, gravity is coming out of the screen and an external magnetic field is entering the screen. a) Shows the accumulation of SS bacteria on the bottom glass. Bacteria appear as points, since they are oriented perpendicular to the plane of view. Some rod shapes are visible, which correspond to MTB with weak magnetic moment. b) NS bacteria accumulation occurring at the top glass.

Figure 1.9 shows snapshots of what was observed after the magnet was put. The red arrow in figure 1.9a), indicates the border of the droplet. It appears as a small white triangle in the upper-left corner of every image. Without the presence of the magnetic field, a dark ring evidences accumulation of bacteria inside the droplet. Once the magnet is put at time $t = 0$, an initially homogeneous suspension starts to generate density heterogeneities, where the dark zones correspond to high densities of bacteria, and the bright zones correspond to low densities. As time evolves, those density differences start to draw cell-like type of patterns, similar to those of Rayleigh-Bénard convection. At the end, the well defined borders of the cells begin to disassemble, leading to a more disperse state at $t = 80\,\mathrm{s}$.

Although this experiment seems to be simple, a lot of uncontrollable variables were present, such as the shape of the drop and its evaporation after being deposited on the glass, or the inhomogeneity of the magnetic field of the magnet. This led to the design of a new robust setup (section 2.2) were the parameters of the experiment are well controlled. Thus, the main objective of this thesis is to characterize the pattern formation in dense suspensions of MSR-1 under confinement, when a homogeneous magnetic field is applied. This includes giving a qualitative description of the phenomena, perform quantitative measurements of the temporal and spatial scales involved in the phenomenon and observe their dependence on the experiment parameters, namely, the concentration of the bacterial suspension, the strength of the magnetic field and the height of the confinement.

Trying to understand why this type of patterns develop under these conditions and thanks to the resemblance of the patterns to those arising from the Rayleigh-Bénard instability, we

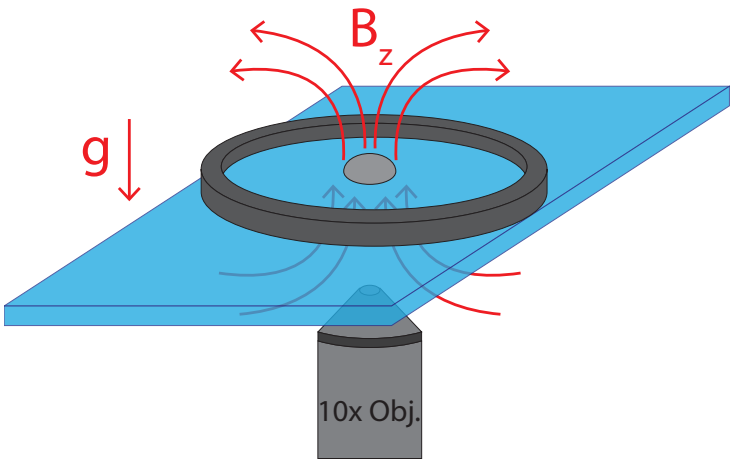


Figure 1.8: Diagram showing the setup of the exploratory experiment. A drop with a dense suspension of bacteria was put on a glass slide to be observed under a microscope. A magnet was placed on the glass, with the drop at its center to let bacteria interact with the magnetic field generated by the magnet. The curved red lines are a representation of how the magnetic field of the magnet could look like. There is not certainty regarding the homogeneity of the field.

stepped upon the phenomenon known as bioconvection. In the next section, a small explanation of bioconvection is given, starting from classical convection and finishing with the physics of the type of collective motion called Magneto-Bioconvection.

## 1.3. Collective motion: Bioconvection

In active systems, large-scale ordering is possible thanks to the interactions between the individuals and the environment as well as the interaction between the individuals themselves. Animals can organize thanks to social interactions among close neighbors in order to, for example, migrate more efficiently to a more favorable weather. Under specific circumstances, cells in tissues release chemicals that can be sensed by other cells to start a process called cell migration, which is essential, for example, in wound healing and in the early stages of animal embryogenesis [Trepat et al., 2009]. At high density, bacteria such as *E. coli* or *B. subtillis* move coherently at length scales larger than the size of its units, exhibiting fluctuating patterns of vortices and jets, in a phenomenon known as active turbulence [Wensink et al., 2012, Peng et al., 2021]. Dense suspensions of *B. subtillis* inside pancake-shaped drops, self-organize into a steady single-vortex state, accompanied by a thin counterrotating boundary layer [Wioland et al., 2013]. Dense suspensions of *E. coli*, when confined inside water-in-oil droplets, are capable of transfering movement to the drop, which performs a persistent random walk [Ramos et al., 2020]. When measuring the shear stress in a low-shear Couette rheometer, bacterial suspensions of *E. coli* display a "superfluidlike" transition, where the viscous resistance to shear vanishes [López et al., 2015].

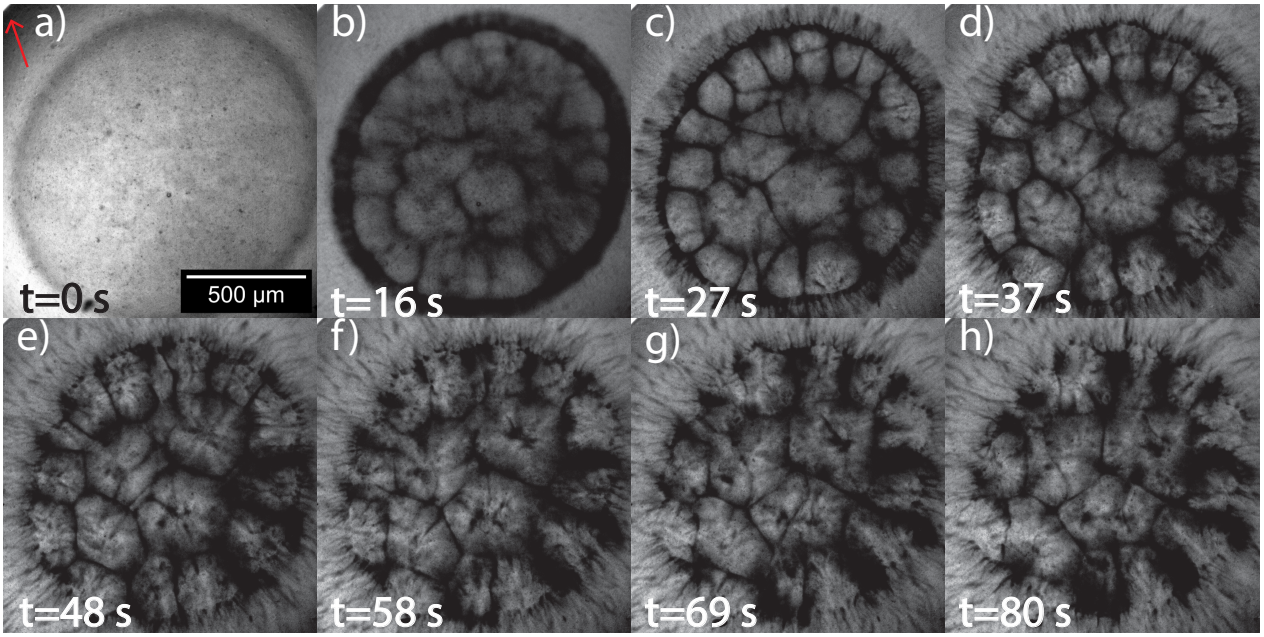


Figure 1.9: Snapshots of a video of a drop with a dense suspension of MTB, affected by the magnetic field of a magnet.

In this section, we will focus on another type of collective behavior known as bioconvection. Coined by Platt in 1961 [Platt, 1961], but reported since 1860, bioconvection owes its name to the resemblance between the patterns formed in some dense suspensions of microorganisms and those of convection systems with a free upper surface (Fig. 1.10).

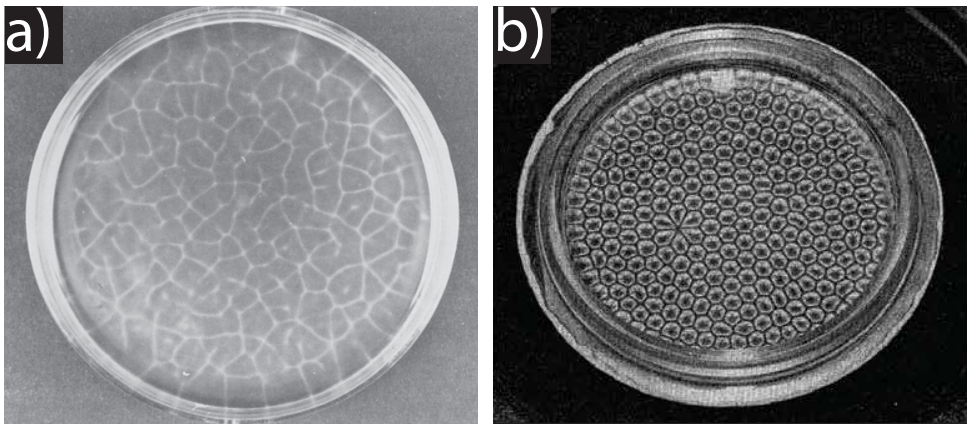


Figure 1.10: Comparison between bioconvection and convection cells. a) A dense culture of *Tetrahymena pyriformis* forming bioconvection patterns. b) Bénard-Marangoni cells formed in a fluid heated from bellow.

Let us first explain how classical convection patterns arise from the Rayleigh-Bénard instability.

### 1.3.1. The Rayleigh-Bénard instability

Consider the following system: a fluid between two plates, located at $z = 0$ and $z = h$ with the $z$ axis pointing anti-parallel to gravity, at temperatures $T_{(z=0)} = T_1$ and $T_{(z=h)} = T_2$ as shown in figure 1.11. For a fluid whose density varies linearly with temperature, according to

$$\rho = \rho_0(1 - \alpha(T - T_0)), \tag{1.3}$$

where $\rho_0$ is the density of the fluid at temperature $T_0$ and $\rho$ is the density at a temperature $T$, with $\alpha > 0$ (meaning, the density decreases with increasing temperature), it is possible to identify two situations. One in which $T_2 > T_1$ and another with $T_1 > T_2$.

In the first case, nothing interesting happens. The system is already in equilibrium with the warm part of the fluid located at the upper side and the cold part below, so no flow is generated.

In the second case, however, since the fluid is being heated from below, the density of a section of the fluid closer to the bottom plate, is lower than those above it. This generates a displacement of the particles from bottom to top. If the moving fluid section does not cool fast enough, its relative density with the surrounding fluid will increase, therefore increasing the movement of the fluid due to Arquimides buoyancy and enhancing convection. Once the fluid particle reaches the top plate, it cools and then moves towards the bottom plate, re-initiating the cycle.

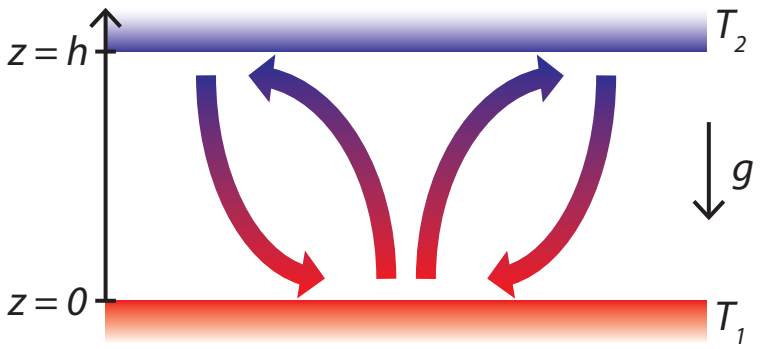


Figure 1.11: Diagram showing the dynamics of the Rayleigh-Bénard instability. The bottom plate heats the fluid, decreasing its density and producing an upward flow. When reaching the top interface, the fluid cools, which increases its density, producing a downward flow. The accumulation of this effect generates re-circulation flows that spread along the zone between the plates.

Whether the instability will appear or not depends on the interplay between thermal transport due to diffusion and thermal transport due to convection. This is quantified by the

*Rayleigh number*, defined as

$$Ra = \frac{\text{time scale of thermal transport due to diffusion}}{\text{time scale of thermal transport due to convection}} = \frac{\alpha \Delta T g h^3}{\nu \kappa}, \tag{1.4}$$

where $\Delta T = T_2 - T_1$, $g$ is the gravity acceleration, $\nu$ is the kinematic viscosity of the fluids, and $\kappa$ is its thermal diffusion coefficient. It has been measured experimentally that the critical value for the Rayleigh number $Ra_c$ for the Rayleigh-Bénard instability to appear is 1708 [Guyon et al., 2015]. Above this number, convection will occur leading to band type of patterns.

If instead of a rigid plate, we consider a free upper surface, another instability appears, known as the Bénard-Marangoni instability. In this case, temperature-dependent surface tension differences are generated in the free surface due to temperature heterogeneities induced by convective flows. Consequently, cells become the stable type of pattern as it is shown in figure 1.10 b).

### 1.3.2. Classical Bioconvection

Bioconvection is the name given to pattern-forming motions resulting from hydrodynamic instabilities in dense suspensions of heavier-than-water micro-organisms [Pedley and Kessler, 1992]. The earliest observations of such phenomena date from the year 1848 [Nägeli, 1860], but a detailed description was given by Wager in 1911 in suspensions of unicellular algae [Wager, 1911]. This type of bioconvection does not require the micro-organism to present a type of sensoring of the environment. Although most of the first experiments to study bioconvection were carried out with phototactic algae, such experiments were performed in absence of light, with gravity and the mass distribution of the cell playing a fundamental role. Here, we will show the mechanism that makes this possible, using as an example the unicellular alga *Chlamydomonas Nivalis*.

*C. Nivalis* is an ovoid-like shaped micro-organism that swims towards its longitudinal axis $\hat{\boldsymbol{n}}$ thanks to the presence of two flagella at the front of the cell (figures 1.12 a) and b)), that are able to perform a "breaststroke" type of movement to propel the cell. It is also said to be a "bottom-heavy" type of cell, meaning that its center of mass (in which gravity $\boldsymbol{F_g}$ acts) is displaced with respect to the geometric center (where buoyancy $\boldsymbol{F_b}$ acts) to the rear of the cell. This feature causes the micro-swimmer to experience a gravitational torque $\boldsymbol{\tau_g}$, orienting it to swim upwards, to develop reverse gravitaxis, meaning that it mainly swims anti-parallel to gravity acceleration.

Let us consider now a vertical shear flow, as the ones showed in figure 1.12 acting on the cell. As shown by John Kessler, the body of the micro-swimmer will experience a viscous

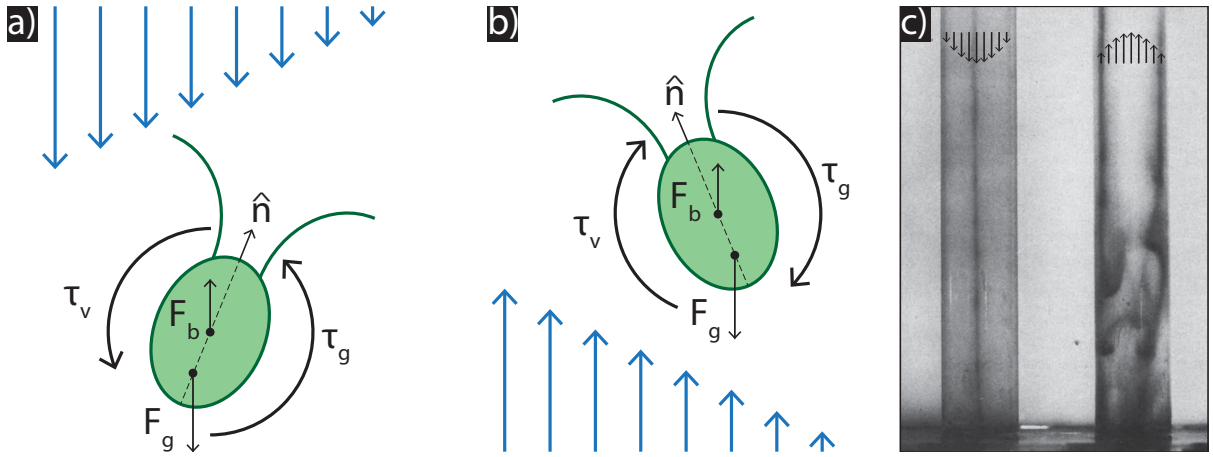


Figure 1.12: a-b) Diagrams showing the mechanism leading to gyrotaxis. c) Image of the experiment carried by Kessler showing the accumulation of cells. When the flow goes downwards, parallel to gravity, accumulation of cells occurs near the center of the tube. When the flow goes upwards, anti-parallel to gravity, cells accumulate at the boundaries of the tube.

torque $\boldsymbol{\tau_v}$ and, depending on the flow going downwards or upwards, it will direct the cell to move towards or away of the increasing flow velocity respectively (figure 1.12a) and b), due to the interplay between the viscous and gravitational torque. This effect is called "gyrotaxis" and was observed experimentally (1.12c) [Kessler, 1985].

The implications of gyrotaxis in the case explained above have a great impact on the overall dynamics of the dense suspension of bottom-heavy micro-swimmers. Going back to the absence-of-flow situation, a small heterogeneity on the density field of cells will provoke the denser part to sink, generating a shear flow that will attract the surrounding micro-swimmers due to gyrotaxis. This is a self-sustained process that explains the downward flow of cells in bioconvection. In the diluted part of the density field, cells swim upwards re-initiating the cycle.

This mechanism is not restricted to unicellular algae, but it is quite ubiquitous in different kinds of "bottom-heavy" cells, such as the ciliated unicellular eukaryote *Tetrahymena pyriformis*, as shown in figure 1.11 a).

For non gravitactic organisms, another type of stimuli is required to generate the upper swimming behavior of the cells. For aerotactic bacteria, this can be achieved by imposing an external oxygen gradient inside a cavity, with the bottom interface being sealed by glass and the upper interface exposed to air. This experiment was carried out by Kessler in 1989 [Hillesdon et al., 1995] in dense suspensions of aerotactic bacterium *B. subtilis*. The mechanism for bioconvection in this setup is similar to that described above. Bacteria swim upward due to an oxygen gradient, generated by the consumption of oxygen in the bulk of the suspension and the free surface in the upper interface, which feeds the suspension with fresh air. Once

the accumulation on an upper region is large enough, density differences lead some spots to sink, generating a downward flow that spreads at the bottom, allowing bacteria to start their upward swim again, re-initiating the cycle (Fig. 1.13).

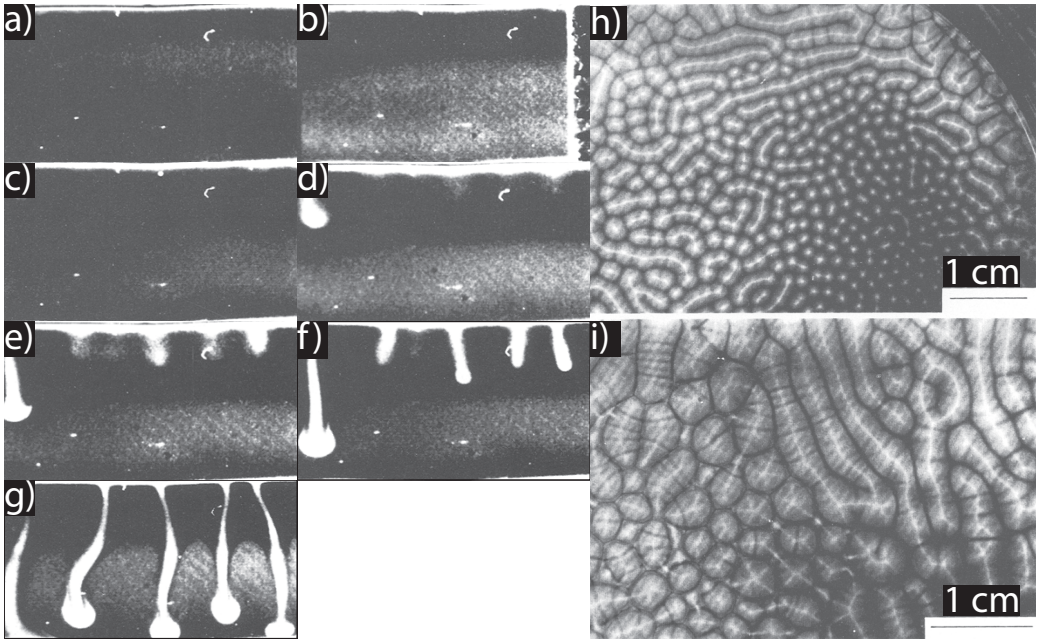


Figure 1.13: Snapshots of bioconvection experiments carried out with aerotatic bacterium *B. subtilis*. a) - g) side view showing the temporal evolution of the instability caused by the accumulation at the top of the cavity of height $h \approx 7 - 8\,\text{mm}$. h) - i) show a top view of a 2.5 mm deep petri dish near the border and the center of the dish respectively. Images taken from [Hillesdon et al., 1995].

Those mentioned above, were some of the first reports regarding bioconvection. This triggered the development of several works, both theoretical [Hillesdon and Pedley, 1996, Pedley and Kessler, 1990, Pedley and Kessler, 1992, Childress et al., 1975, Hill et al., 1989, Vincent and Hill, 1996, Bees and Hill, 1997], numerical [Yanaoka et al., 2009, Yanaoka and Nishimura, 2022] and experimental, using different types of micro-organisms, such as *C. nivaris* [Kessler, 1985, Pedley and Kessler, 1992, Kessler, 1986, Wager, 1911], *Euglena viridis* [Wager, 1911], *B. subtilis* [Jánosi et al., 1998, Hillesdon et al., 1995], *T. pyriformis* [Plesset and Winet, 1974] and MTB [Pierce et al., 2020, Théry et al., 2020]. The latter will be explained in more detail in section 1.3.3.

It is thought that bioconvection helps to deliver food and oxygen to places where normally they would not be available, but there is no strong evidence to support that [Jánosi et al., 2002]. A deep understanding of bioconvection can improve the production of biofuels by taking into account the macroscopic behavior of this micro-swimmers [Bees and Croze, 2014].

### 1.3.3. Magneto-Bioconvection

It was already mentioned in section 1.1.1 that microswimmers can be one of two kinds, a pusher or a puller. MTB can be of both types, but the works that will be shown in this section, were carried out using pusher types of MTB.

Inside a cylindrical cavity, a diluted suspension of magnetotactic bacteria *Magnetospirillum magneticum* can generate density clusters when exposed to an external magnetic field [Pierce et al., 2020]. The mechanism goes as follows. A magnetic field in the direction perpendicular to the surface is imposed, forcing MTB to orient their swimming direction towards a wall. When meeting it, MTB are trapped in the direction of the external field, but still being able to swim along the wall. If two cells are close enough, they will be affected by the flow field of the other cell and, since they are pusher microswimmers, they will attract each other from the sides. This initial cluster will attract more and more cells, increasing its size until there are no more cells to lure. The flow generated by one cluster has the shape of the flow generated by a large pusher type of cell, meaning that it attracts the fluid from the sides and pushes it from the rear, as shown in figure 1.14. It is worth mentioning that the same effect has been recreated for *M. Gryphiswaldense* MSR-1 in our lab, showing, qualitatively, the same behavior.

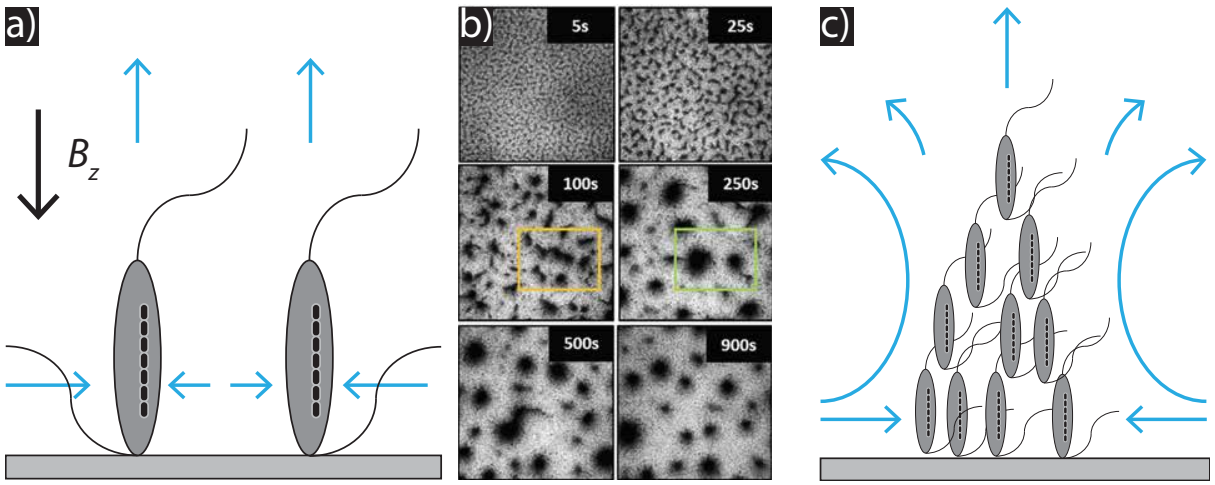


Figure 1.14: Accumulation of MTB near a surface causes them to attract each other, forming clusters. a) Schematic of the flow of two neighbors cells. Given their pusher nature, they pull fluid from the sides, attracting one another. b) Time evolution of the formation of clusters. From the moment a magnetic field is applied perpendicular to the plane of view, attraction starts to occur. c) Schematic of the flow field of the clusters.

In another experiment, a dense suspension of *M. gryphiswaldense* was observed inside a square glass capillary, with an external magnetic field applied perpendicular to gravity and to the capillary's long axis, as shown in figure 1.15 [Théry et al., 2020]. In accordance with the experiment described above, once bacteria start to accumulate in the walls, they attract

each other forming a bigger structure. This can be interpreted as a cluster seen from the side. A detailed observation of the flow generated by the accumulation of cells, shows that the formed structures resemble a convection plume, hence, the name "magneto-bioconvection". This is different from the classical bioconvection described in section 1.3.2, since classical bioconvection depends on a density mismatch between layers of the fluid affected by gravity. In this experiment, gravity is not relevant. The resulting plumes appear due to the addition of the flow fields of individual cells.

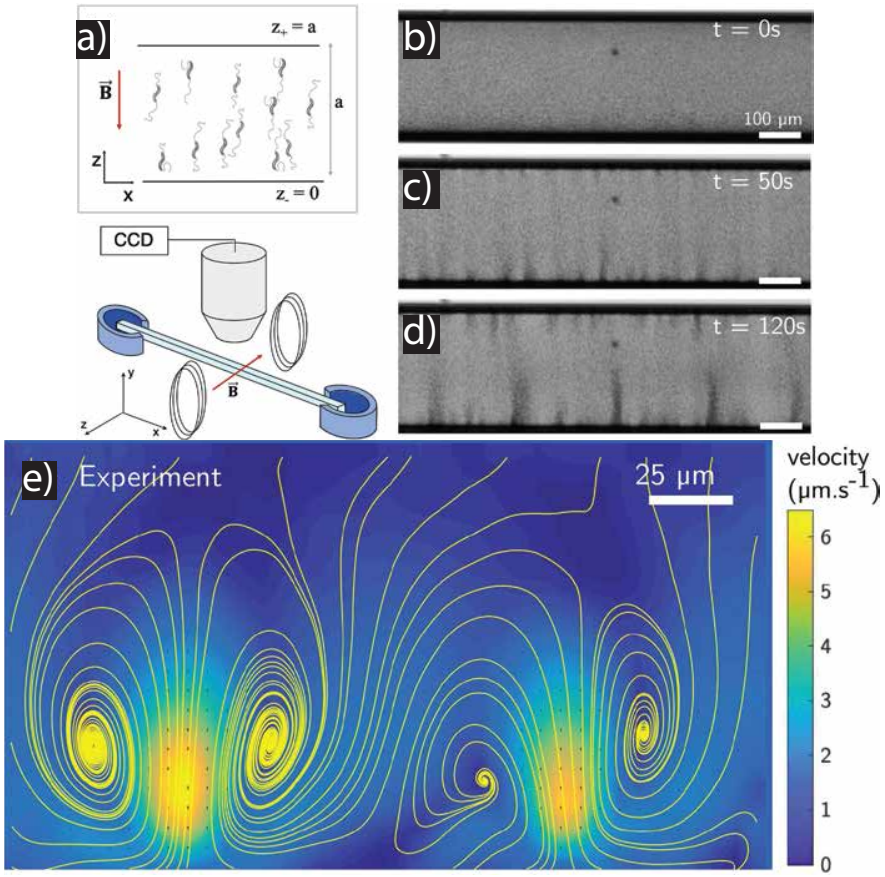


Figure 1.15: Observation of magneto-bioconvection plumes. This experiment shows a side view of the clusters formed in [Pierce et al., 2020] (fig. 1.14). This allowed the measurement of the velocity field, which corresponds to a convection flow. a) Diagram of the experiment. A homogeneous magnetic field, perpendicular to gravity, is generated inside a glass capillary with square cross section, with its long dimension oriented perpendicular to the magnetic field, containing a dense suspension of north-seeking MTB. b-c-d) Time evolution of the experiment, showing the formation of plumes. The distance between plumes is comparable to the size of the capillary tube. e) Flow-field of the plumes.

In another work, experiments consisting of a dense suspension of MTB, confined in water-in-oil droplets (figure 1.16a) were performed. When a magnetic field is applied in a direction perpendicular to gravity, MTB self-assemble into a rotary motor, capable of exerting a torque

over the external oil phase (figure 1.16 b). This is possible thanks to the formation of two diametrically opposing jets (figure 1.16 c), one composed mainly by NS bacteria, and the other one by mainly SS bacteria. As density of bacteria increases inside the droplet, the interaction between those jets leads to the formation of a vortex (figure 1.16e). The jets can be seen as magneto-bioconvection plumes, whose interaction is strictly related to the geometry of the confinement.

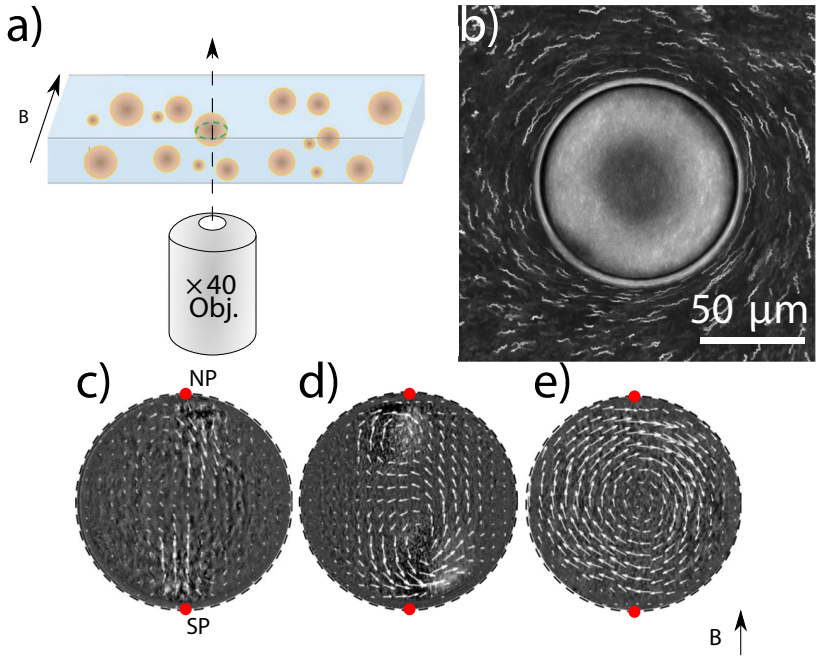


Figure 1.16: Confined MTB inside water-in-oil droplets self-assemble into rotary motors. a) Diagram of the experiment. A magnetic field is applied parallel to the plane of view. b) Superposition of confocal fluorescence images, showing the circular rotation of tracers outside the droplet. c-e) Particle image velocimetry inside the droplet with densities increasing from c) to e).

# Chapter 2

# Methods

As mentioned in section 1.1.3, bacteria constitute a very useful system to be studied in the laboratory. Since *M. gryphiswaldense* MSR-1 is the chosen organism to work with, all the necessary protocols to grow them needed to be learn. It was also necessary to fabricate the setup to observe and steer the bacteria movement, consisting of confinement cavities and Helmholtz coils to generate magnetic fields. In this section both processes are explained.

## 2.1. Culture of *Magnetospirillum Gryphiswaldense*

The culture of magnetotactic bacteria begins with a sample taken from an ultrafreezer at $-80\,^{\circ}\mathrm{C}$, to then be grown at the specific conditions they need, which in this case is a culture medium called *Flask Standard Medium*.

### 2.1.1. *Flask Standard Medium* preparation

*Flask Standard Medium* (FSM), is a solution that contains all components required for the reproduction and growth of MSR-1 in addition to provide the minerals for the development of the magnetosome (1.1.3).
To prepare the FSM, the following reagents are mixed in a 1 L bottle:

1. 10 mL of Hepes buffer
2. 3.8 mL of Potassium lactate solution
3. 3 g of Soy peptone
4. 0.1 g of Yeast extract
5. 1 mL of $KH_2PO_4$ solution
6. 4 mL of $NaNO_3$ solution
7. 6 mL of $MgSO_4$ solution

8. 5 mL of Ferric citrate solution

To make 12 mL of reagent 2, it is necessary to mix 10 mL of Potassium lactate and 2 mL of distilled water. The Potassium lactate already comes in a 60 % aqueous solution.

In order to integrate the reagents 5, 6, 7 and 8, it is required to dilute them in distilled water, following the next quantities, respectively:

- 1 g of $KH_2PO_4$ in 10 mL of distilled water
- 1 g of $NaNO_3$ in 10 mL of distilled water.
- 0.246 g of $MgSO_4 7H_2O$ in 10 mL of distilled water.
- 0.25 g of Ferric citrate in 10 mL of distilled water. The solution is mixed using a magnetic stirrer and heat, until it turns from a cloudy and brownish color, into a transparent yellowish liquid.

After mixing the reagents, 970 mL of distilled water are added.

To finish the process, the FSM is filtered and sterilized using Nalgene filters. The content is stored at 4 °C for further use.

Since MSR-1 needs micro-aerobic conditions to grow, it is necessary to inoculate them in an environment isolated from atmospheric air. For that, 12 mL of FSM are deposited in a Hungate tube. The content is then bubbled with $N_2$ using a hose, leaving a gap with the ruber cap for air to escape the tube, as shown in figure 2.1. After 60 seconds of bubbling, the hose is removed, while keeping the rubber cap from moving. Once the hose is out of the tube, it is closed immediately with the rubber cap and then sealed firmly with the plastic cap.

Finally, the tube is autoclaved. Once the temperature is lowered to room temperature, the FSM is ready to use.

### 2.1.2. MSR-1 inoculation

For the inoculation of bacteria, these steps are followed:

- A cryotube with bacteria stored at −80 °C is taken to room temperature and the content is allowed to melt.
- In the laminar flow hood, the rubber cap of the Hungate tube is washed with pure ethanol. Then it is light with fire.
- In the laminar flow hood, 300 $\mu$L of bacteria stock are taken from the cryotube, using a sterile syringe, and inoculated into the FSM, as shown in figure 2.2.

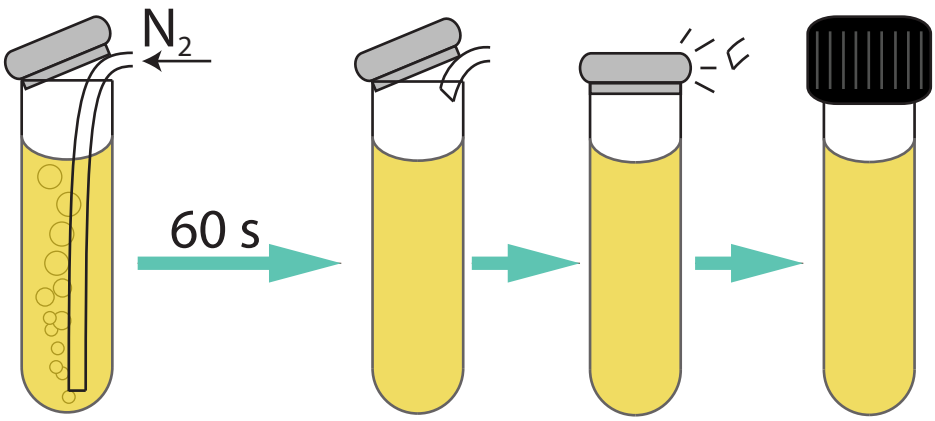


Figure 2.1: Diagram of the bubbling process of FSM. First, the content is bubbled using a hose while holding the rubber cap over the hose. After 60 seconds, start taking the hose out of the tube, being careful not to lift the rubber cap. As soon as the hose is out of the tube, the rubber cap is closed and then reinforced with a plastic cap.

- The Hungate tube is left in the incubator, at 28 °C and shaked at 180 RPM.
- After 48 hours, the culture should be in good conditions of density (measured by means of optical density at 405 nm, $OD_{405} \approx 0.2 - 0.3$) and motility to be used in experiments.

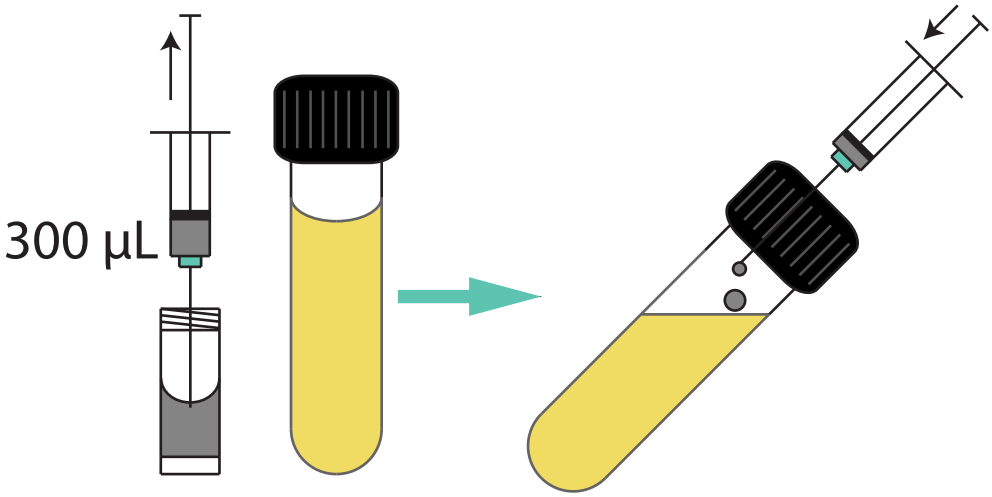


Figure 2.2: Diagram of the inoculation process. Under a laminar flow hood, 300 µL of bacteria are taken from a cryotube once the content melts, and inoculated into a Hungate tube prepared according to the process explained in subsection 2.1.1. For the inoculation it is necessary to tilt the tube, so the drops of bacteria fall directly over the FSM and not over the glass.

### 2.1.3. Dense suspension generation

The hungate tube content is poured into a 15 mL Falcon tube and centrifuged at an acceleration of $\approx 2750g$ for 5 minutes. Next, the supernatant is taken out, leaving a volume comparable to the volume of the dense fraction of bacteria inside the tube, as shown in figure 2.3. Then, the content is re-suspended carefully, using a micro-pipette. The result is a suspension of MTB denser than that of the initial tube. The optical density of the suspension is measured using an optical spectrometer, by diluting 5 µL of it, in 1 mL of FSM, obtaining values of $OD_{405} \in [26, 129.1]$. The rest is ready to be used in experiments.

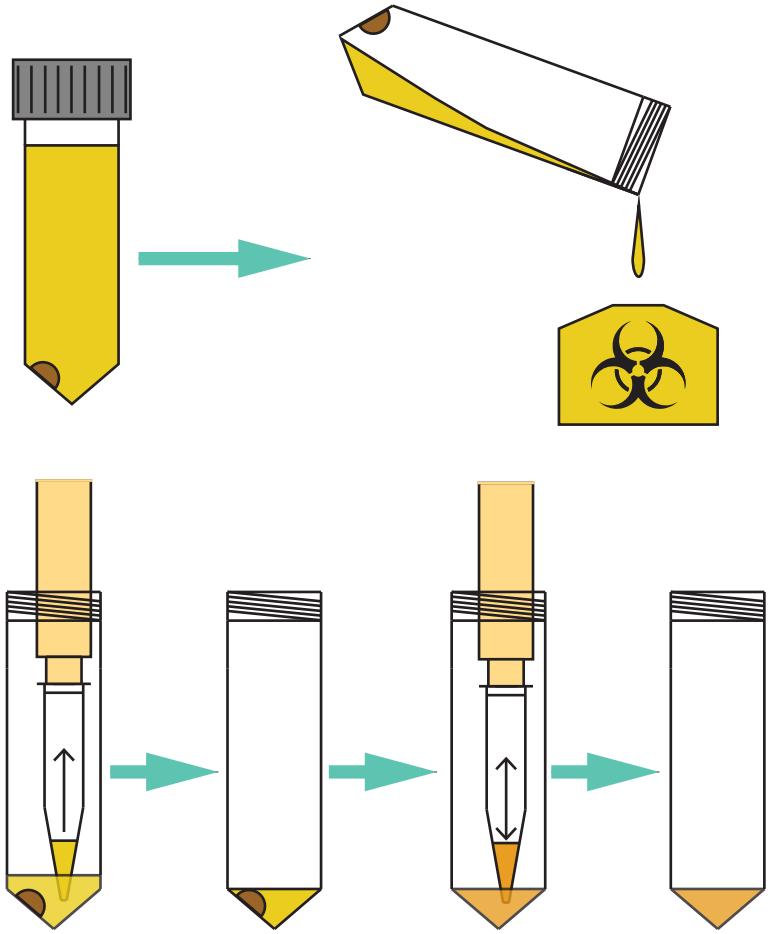

Figure 2.3: Diagram of the bacteria concentration process. After being accelerated in the centrifuge, a small brownish volume ("pellet") will appear at the tip of the falcon tube. This corresponds to a high density suspension of bacteria. The supernatant is carefully poured in a bio-waste container, leaving a small volume of supernatant in the tube, comparable to the volume of the dense fraction. Part of the residual supernatant is removed using a micro-pipette, being careful not to extract the pellet. The most supernatant is removed, the denser will be the final suspension but the smaller will be the volume. Finally, the fluid is re-suspended with a micro-pipette, this time, being careful not to generate bubbles.

### 2.1.4. Stock

In order to keep a permanent stock of MSR-1, a $-80\,^{\circ}\mathrm{C}$ freezer is used to store bacteria for long periods of time. These are the steps to prepare the stock:

- A bacterial culture is prepared, as indicated in sections 2.1.1 and 2.1.2, and the bacterial motility is evaluated before continuing.
- If motility is good, 1000 µL of bacterial culture are mixed with 400 µL of a mixture of Glycerol and FSM 60/40 v/v inside a cryotube. The cryotube is manually agitated and placed inside liquid nitrogen.
- The cryotube is removed from the liquid nitrogen and placed inside the $-80\,^{\circ}\mathrm{C}$ freezer.

### 2.1.5. Density calibration

Optical density (OD) is a dimensionless quantity that measures the amount of light absorbed by cells in a fluid sample, that can be related to the number of cells in a suspension. The wavelength of the light can be tuned depending on the size of the elements that one wants to measure. We determined that the optimal absorption of a bacterial suspension of *M. Gryphiswaldense* occurred with an incident light of 405 nm.

To relate the number density of bacteria with optical density values, various tubes with suspensions of bacteria at different densities were prepared and their OD was measured. Small volumes of the samples (10-20 µL) were extracted and deposited in a Neubauer Counting Chamber, which consists on a grid-patterned glass cavity with fixed height and grid dimensions (figure 2.4a). Consequently, each cell of the grid has a well known volume of $4 \times 10^{-3}$ µL. The number of bacteria observed inside three different cells as the one shown in figure 2.4b) was counted for each sample using a 60x objective lens in a microscope, thus, obtaining a value for the number of bacteria per unit volume $n$. Figure 2.4c) shows the dependence of $n$ on the $\mathrm{OD}_{405}$.

A linear regression was performed to the data, giving the relation $n = \mathrm{A}\ \mathrm{OD}_{405}$, where $\mathrm{A} = 1.74 \times 10^5\,\mathrm{bac/\mu L}$. The experiments performed here had optical densities from 26 to 129.1, giving number densities ranging from $4.5 \times 10^6$ to $2.12 \times 10^7\,\mathrm{bac/\mu L}$.

## 2.2. Experiment

The number density of MTB can be controlled using the protocol explained in section 2.1.3. For this experiment we inoculated (deposited) a dense suspension inside a cylindrical cavity of height $h$ (section 2.2.1), covered with a glass slide. The inoculated cavity was then placed between a pair of Helmholtz coils, a device capable of generating homogeneous magnetic fields $B_z$ on the direction anti-parallel to gravity, as shown in figure 2.5. Videos ranging

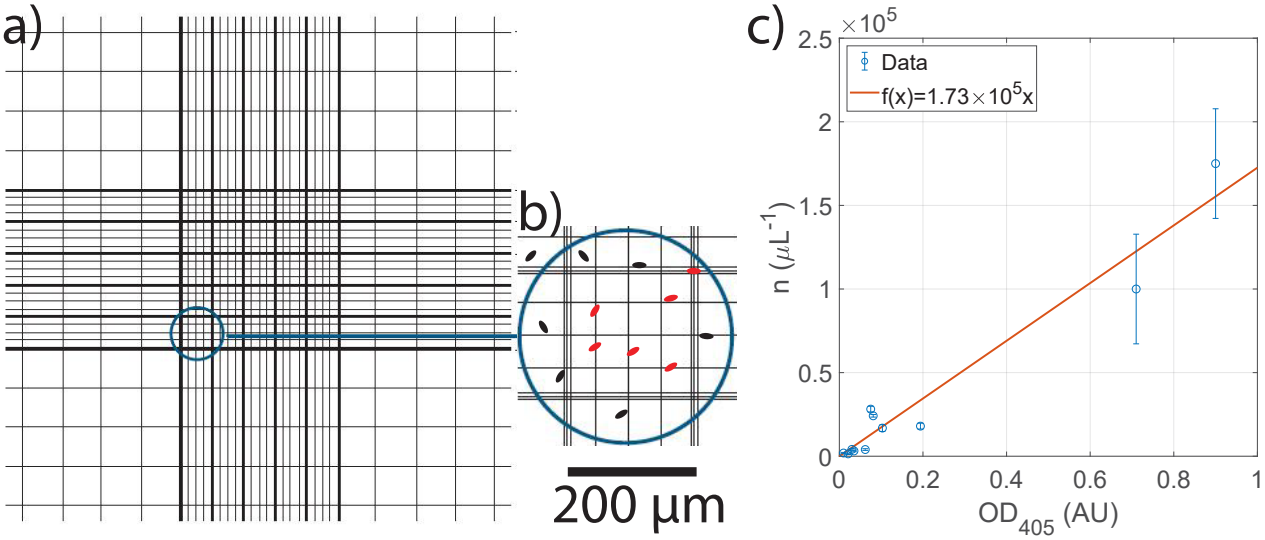


Figure 2.4: a) Diagram of the grid patterned in a Neubauer Chamber. b) Observed cell that fits the field of view of a 60x objective lens, where the bacterial cells represented as red dots were counted. The black dots represent bacteria outside of the counting cell, thus, they were not counted. c) Number density of bacteria as a function $OD_{405}$. The linear fitting determines the conversion from $OD_{405}$ to $n$.

from 5 to 15 min of duration were recorded in order to capture the evolution of the system from the moment the magnetic field was turned on.

To prepare the experimental set-up, it was necessary to fabricate both the micro-cavities in which bacteria were deposited and the coils system to generate the homogeneous magnetic field. The former will be explained in section 2.2.1 and the latter in section 2.2.2.

### 2.2.1. Micro-fabrication

The confinement was imposed by the fabrication of two types of cavities.

The first one was the simplest. Double-sided adhesive tapes, of thickness $h \sim$ 50-110 µm, were cut to match the size of a glass slide. Then, they were pierced with a hollow punch, leaving the tapes with a hole at its center. For the experiments, the cavities were taped to a glass slide, filled with a dense suspension of bacteria (section 2.1.3) and covered with another glass slide.

The second type of cavities were made of Polydimethylsiloxane (PDMS), a silicon-based polymer with a variety of properties such as hydrophobicity, optical transparency and good gas permeability. To obtain the desired form and height, the cavities were shaped from a resin mold, previously fabricated using conventional optical lithography.

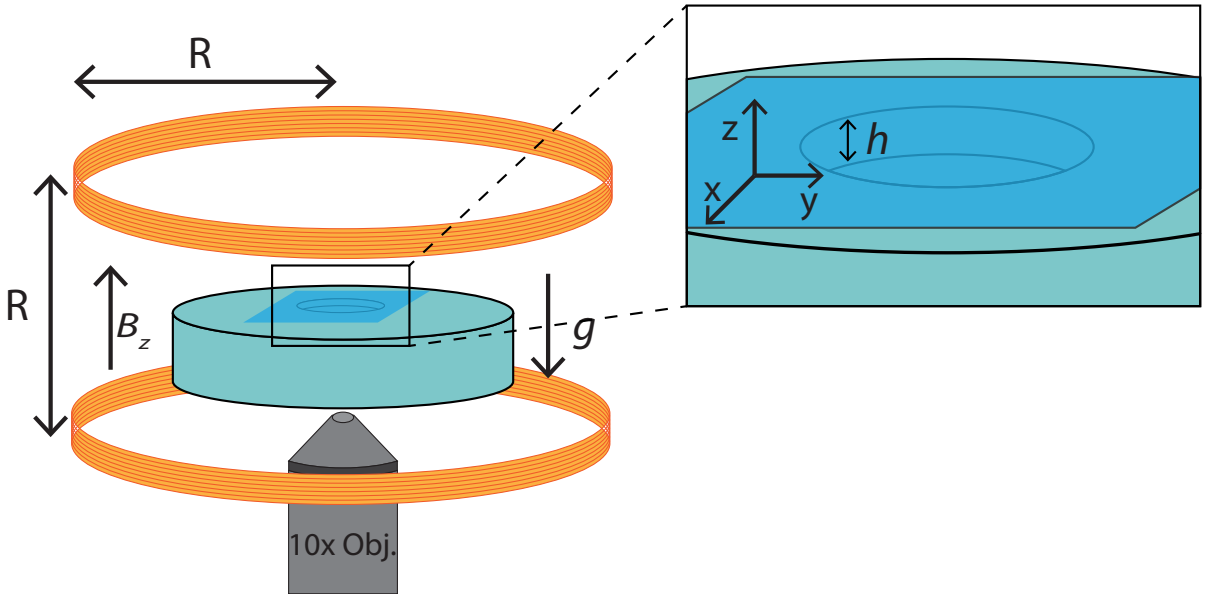


Figure 2.5: Diagram of the experimental set-up. A dense suspension of magnetotactic bacteria is deposited inside a cylindrical cavity, of height $h$ and then covered with a glass slide. A homogeneous magnetic field $\vec{B_z}$ is applied to the sample. Bacteria behavior is observed from bellow through an inverted microscope.

The process begins by cleaning a 2 inch silicon wafer with a plasma cleaner for 8 min, which uses ionized gases to clean the surface of the wafer from organic contamination. Then, a photocurable epoxy called SU-8, is added in liquid form over the wafer, covering up to two thirds of its area from the center out. In order to reach a specific thickness of the SU-8 layer, the wafer is rotated using a spin coater. The final thickness will depend on the type of SU-8 (specifically on its viscosity), the time and speed of rotation. A summary of all the process is shown in table 2.1. In this case, the same epoxy is used for the three desired thicknesses.

The second step is called pre-bake, and its objective is to evaporate the solvents from the SU-8 layer by placing the wafer on a hot plate. Then, the sample is ready to be exposed to a UV laser that draws a specific design in the epoxy layer. It works by inducing the reticulation of the exposed zones of the SU-8, so in the developing process, the illuminated parts will remain while the rest will dissolve. Before that, it is necessary to make a second baking step, which finishes the reticulation process initiated by the UV laser.

After the post-baking, the wafer is submerged in a bath of propylene glycol monomethyl ether acetate (PGMEA) for a specific time depending on the thickness of the mold. The idea is to dissolve the non-exposed zones of the SU-8 layer, creating the wanted three-dimensional structure over the silicon wafer.

The process finishes with a hard-baking process, of 2 h at 135 °C, to flatten any undesired

Table 2.1: Summary of the fabrication of the resin mold.

| Desired thickness<br>SU-8 | 50 µm<br>GM 1070 | 100 µm<br>GM 1070 | 200 µm<br>GM 1070 |
|---|---|---|---|
| Spin coating 1<br>Spin coating 2 | 60 s at 500 RPM<br>40 s at 1700 RPM | 60 s at 500 RPM<br>40 s at 900 RPM | 60 s at 500 RPM<br>40 s at 400 RPM |
| Pre-bake | 15 min at 65 °C,<br>35 min at 95 °C | 15 min at 65 °C,<br>2 h at 95 °C | 30 min at 65 °C,<br>4 h at 95 °C |
| Exposure dose mJ/cm$^2$ | 800 | 1000 | 1300 |
| Post-bake | 15 min at 65 °C,<br>40 min at 95 °C | 15 min at 65 °C,<br>40 min at 95 °C | 15 min at 65 °C,<br>40 min at 95 °C |
| Development time | 4 min | 5 min | 22 min |
| Hard-bake | 2 h at 135 °C | 2 h at 135 °C | 2 h at 135 °C |

crack and strengthen the adherence between the SU-8 and the silicon wafer.

A summary of the process and all the different parameters for each step, for the three different sizes, are specified in table 2.1.

Once the resin mold is fabricated, it is placed inside a petri dish, waiting for PDMS to be deposited.

PDMS comes originally in liquid form and separated in two components: the PDMS itself and the cross-linking agent, which need to be mixed in a 10:1 mass ratio. After mixing, there is a time window of 48 hours at 25 °C before it cures and solidifies. This time can be reduced up to 10 min by increasing the temperature to 150 °C. Within this time window, it is put inside a void chamber in order to extract as many bubbles as possible. When the sample looks bubble clean, it is left to cure at a desired temperature in a leveled surface. Once cured, the PDMS is cut and taken out of the resin mold, ready to be used in experiments. The resin mold is stored for further fabrications. A diagram showing how the resulting PDMS piece is extracted from the mold is shown in figure 2.6.

The two types of chambers are not equivalent for the experiment. Their main difference concerns the oxygen diffusion from the environment towards the bacterial suspension. Glass does not allow oxygen to penetrate inside the cavity while PDMS does, leading to a higher ventilation in the PDMS cavity compared to the one made with the doubled-sided adhesive tape. The effects of this difference over the bacterial suspension will be discussed in the results, in chapter 3.

All the experiments with a confinement size $h$ =50 µm, were carried out with double-sided tape. For $h$ =100-110 µm, some experiments were made with double-sided tape and some

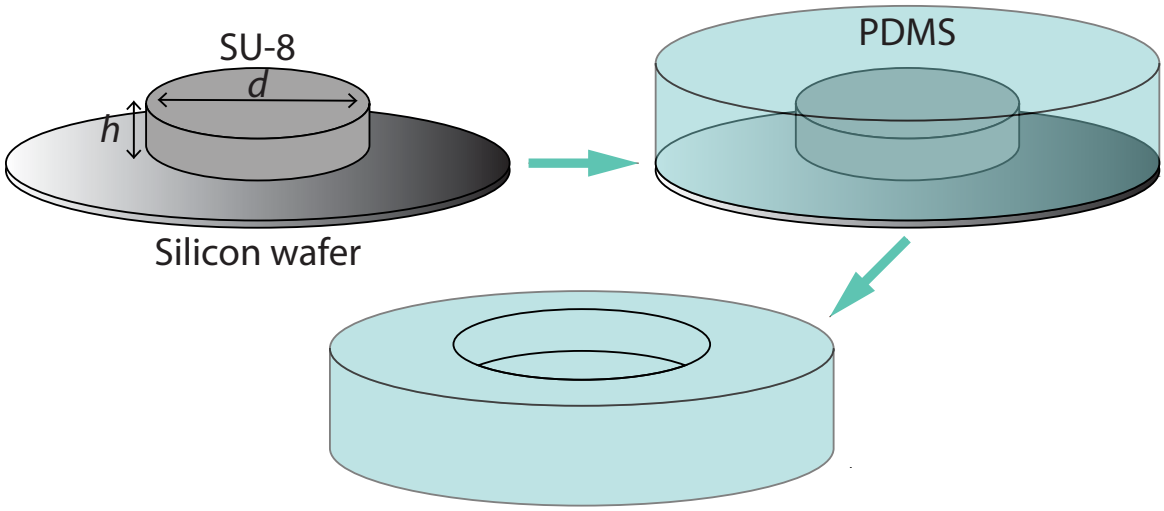


Figure 2.6: Diagram representing the process in which the final PDMS cavity is extracted from the SU-8 mold. First, the negative is filled with PDMS inside a petri dish. Once the polymer has solidified, it is extracted from the petri dish, separating it from the silicon wafer.

with PDMS. The experiments with $h$ =200 µm, were all performed with PDMS cavities.

### 2.2.2. Helmholtz coils fabrication

A system composed of two coaxial current rings, separated by a distance equal to their radius, is called Helmholtz coils. When connected in series, they generate a homogeneous magnetic field at the mid-plane between the coils, which is proportional to the current intensity passing through the coils. For the realization of the experiment, we fabricated a system that could be attached to the microscope of the set-up explained in section 2.2.

The attachment was composed of three parts: a base that fits in the microscope and holds the sample; a bottom frame, attached to the base from below, around which a copper wire was rolled up; and a top frame, set on top of the base around which another copper wire was rolled up. Photographs of the system, and how it is mounted in the microscope, are shown in figure 2.7.

Some experiments were performed using 3D printed pieces. That led to the deformation of the base due to the heat generated by the current flowing through the coils, which caused a displacement of the sample and a subsequent change in the plane of focus. Given that, because of its resistance to deform under temperature changes within the regime of this experiment, the base and the frames were made of duralumin.

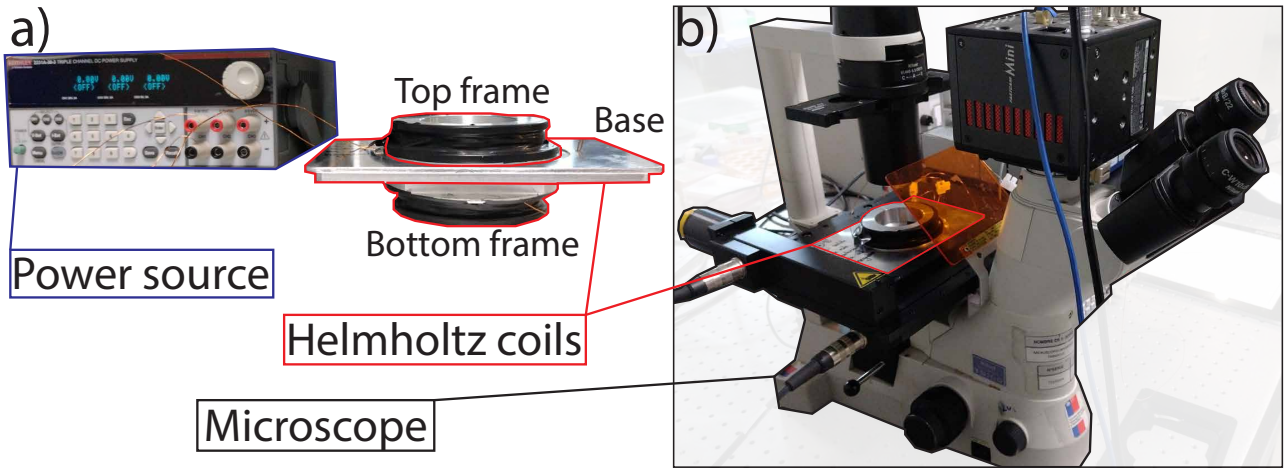


Figure 2.7: Helmholtz coils mounted on the microscope. a) Photograph of the power source and the Helmholtz coils, composed of a base and two frames of duralumin, seen from the side and detached from the microscope. The power source feeds current to the coils to generate a homogeneous magnetic field. b) Photograph of the Helmholtz coil mounted on the microscope.

The intensity of the magnetic field $B_z$ as a function of the current intensity is shown in figure 2.8. For this experiment, magnetic fields were generated, from 2 to 8 mT. Those intensities correspond to around 100 times the earth magnetic field, which typically ranges between $2 \times 10^{-2}$ and $6.8 \times 10^{-2}$ mT [Lanza and Meloni, 2006].

## 2.3. Image analysis: auto-correlation function

When recording a realization of an experiment, several images were obtained, corresponding to different frames at different times. Let us define an image $I''(t)$ of an experiment as a matrix of $M$ by $N$, where each element $I''_{m,n}(t)$ represents a pixel whose value is an integer from 0 to 255, associated with the grayness of that specific pixel, with 0 being total black and 255 being total white, at a given time $t$. For the analysis, the images were post-processed. First, a background image $I''(0)$, corresponding to the homogeneous initial state, was subtracted, giving a new matrix given by

$$I'(t) = I''(t) - I''(0). \tag{2.1}$$

This eliminates any undesired illumination heterogeneity present at the moment of recording the experiment. Then, in order to guarantee a null average, the mean value of $I'(t)$ was subtracted to itself, such as

$$I(t) = I'(t) - \langle I'(t) \rangle, \tag{2.2}$$

where the brackets denote spatial average. An illustrative example is shown in figure 2.9, where an image with periodic structures of a certain size and separation was operated accor-

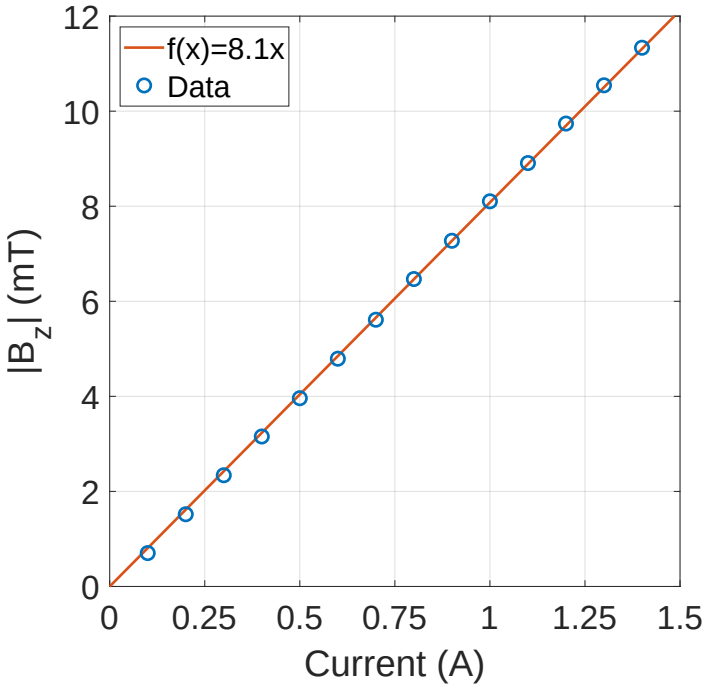


Figure 2.8: Helmholtz coils calibration. The intensity of the magnetic field $B_z$ depends on the current flowing though the wires, giving a calibration coefficient of $8.1\,\mathrm{mT\,A^{-1}}$.

ding equations 2.1 and 2.2. Also, given the quasi-one-dimensionality of the image, the signal was averaged in the $y$ direction.

The auto-correlation function corresponds to a matrix $C(t)$ of $2M-1$ by $2N-1$. The elements of $C(t)$ will be given by

$$C_{k,l}(t) = \sum_{m=1}^{M}\sum_{n=1}^{N} \bar{I}(t)_{m,n}\bar{I}(t)_{M-k+m,N-l+n}, \tag{2.3}$$

where $k \in [1, 2M-1]$, $l \in [1, 2N-1]$ and

$$\bar{I}_{m,n}(t) = \begin{cases} I_{m,n}(t) & \text{if } m \in [1,M] \wedge n \in [1,N] \\ 0 & \text{if not.} \end{cases}$$

Computing $C_{k,l}(t)$ from $I_{m,n}(t)$ can be seen as superposing the image with itself and displacing one with respect to another. When $k = M$ and $l = N$, we are located at the center of the auto-correlation function matrix, meaning that there is no displacement so the value $C_{M,N}$ is maximum. For values of $k > M$ ($l > N$), one of the images is being displaced vertically (horizontally) upwards (to the right) with respect to the other. For values of $k < M$ ($l < N$), one of the images is being displaced vertically (horizontally) downwards (to the left) with respect to the other. If for some displacement, there is a structure that coincides with

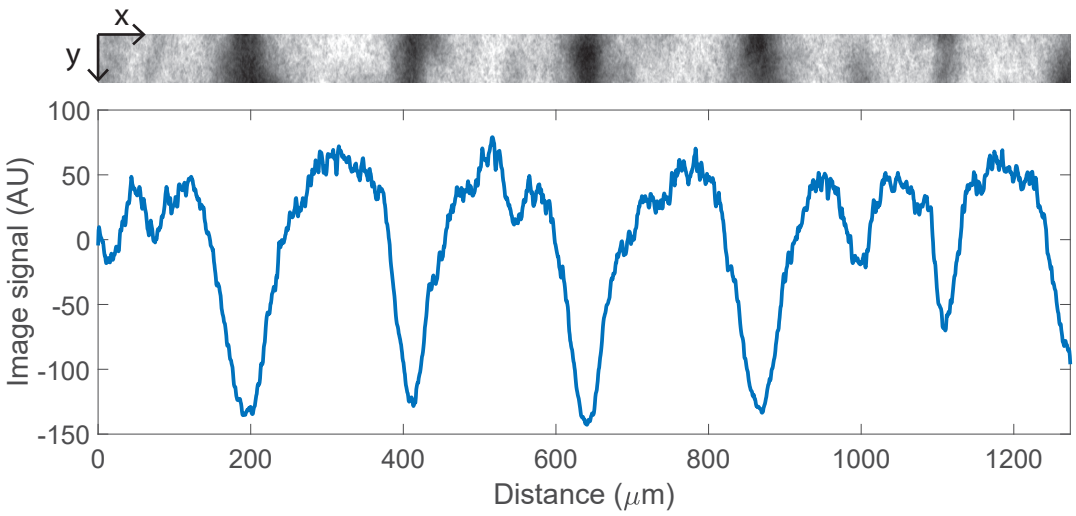


Figure 2.9: Original image and the final signal obtained after the treatment explained in 2.2.

another structure, $C_{k,l}$ will have a local maximum, and the image is said to have a spatial correlation. A local minimum can also be found, so the image has a spatial anti-correlation. Also, since the signal in figure 2.9 goes from positive values to negative values near the border of the periodic structures, the points at which $C_{k,l}$ is zero, will give information of the width of the structures. Figure 2.10 illustrates that.

The value in the $x$-axis at which the auto-correlation function intersects zero, will be denominated $\delta$. This will correspond to the characteristic size of the structure, since zero-valued pixels are more likely to be found at the edges of the structures thanks to the treatment given by equations 2.1 and 2.2. The value on the $x$-axis at which the function has a local minimum, corresponds to $\epsilon$, and it gives information regarding the distance between darker zones and the subsequent brighter zones. Finally, $\lambda$, which corresponds to the value on the $x$-axis at which the function has a local maximum, will contain information regarding the distance at which the structure most assimilates itself, giving as a result a characteristic separation between the structures.

When applying the auto-correlation function over a two dimensional data set such as a frame of an experiment at time $t$, as the one shown in figure 2.11 (instead of the one dimensional signal exemplified in figure 2.10), a two dimensional auto-correlation function is obtained, as it is shown in figure 2.11b). In order to extract a characteristic length scale, the origin was set to be at the center auto-correlation function, where it is its maximum. Given the symmetry of the auto-correlation function, the analysis zone was reduced and only the first and second quadrant were considered, drawn by a segmented line in figure 2.11b).

Several radii were defined to observe transverse cuts of the auto-correlation function defined by each radius. Figure 2.12a) shows $r$ for different inclination angles ($\theta = \frac{\pi}{4}, \frac{\pi}{2}, \frac{3\pi}{4}$) with

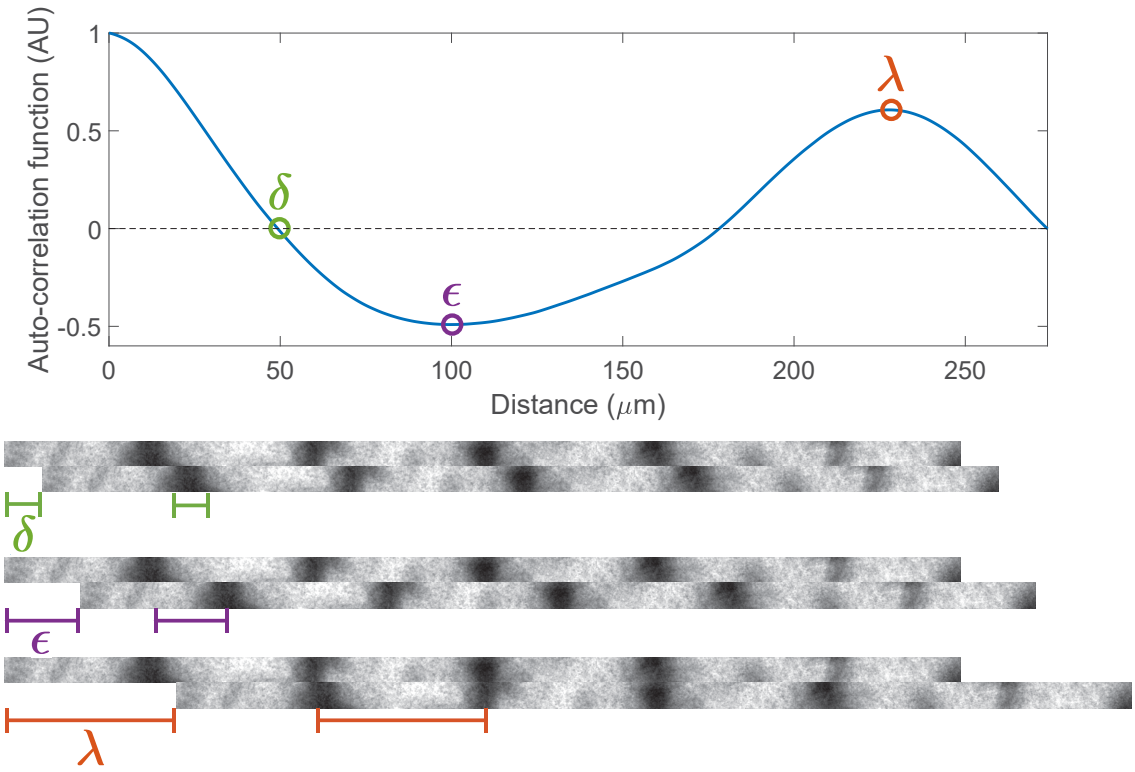


Figure 2.10: Auto-correlation function visualized as a displacement of the image with respect to itself. $\delta$ will give information of the structure size. $\epsilon$ corresponds to the distance between brighter and darker spots. $\lambda$ corresponds to the separation between structures, that being, the predominant wavelength of the pattern.

their respective auto-correlation curves (figures 2.12c), d) and e) respectively). A total of 181 radii between 0 and $\pi$ were analyzed for each frame, where the analysis explained above was performed, obtaining a value $\delta_\theta(t)$ and $\lambda_\theta(t)$ for each $\theta$. The location of those values in the two dimensional auto-correlation function are shown in figure 2.12b).

If $C_\theta(t)$ is the value of the normalized auto-correlation function corresponding to the local maximum $\lambda_\theta(t)$ for an angle $\theta \in [0, \pi]$, a characteristic separation for a frame at time $t$, $\lambda(t)$, can be computed by means of a weighted average, following the formula

$$\lambda(t) = \frac{\sum_\theta C_\theta(t)\lambda_\theta(t)}{\sum_\theta C_\theta(t)}. \tag{2.4}$$

The value of $\lambda(t)$ is illustrated as the radius of a semi-circle, centered at the origin, shown with a segmented orange line in figure 2.12b).

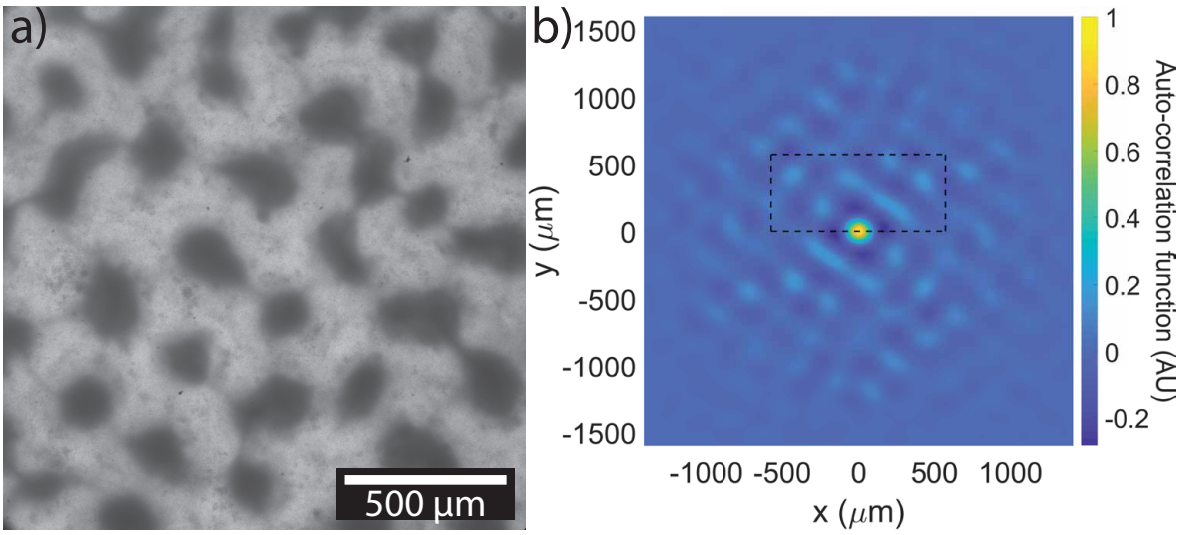


Figure 2.11: a) Frame of an experiment where a two dimensional pattern is observed. b) Two dimensional auto-correlation function computed from the image. The analysis zone was reduced to the zone inside the segmented line.

The value of $\delta(t)$ was calculated as the average of all $\delta_\theta(t)$, according to the formula

$$\delta(t) = \frac{1}{181} \sum_{\theta} \delta_\theta(t). \tag{2.5}$$

The value of $\delta(t)$ is also illustrated as a green segmented line, describing a semi-circle centered at the origin, of radius $\delta(t)$.

The calculations of $\delta(t)$ and $\lambda(t)$ were applied to all frames of the experiments. The results obtained will be shown in chapter 3.

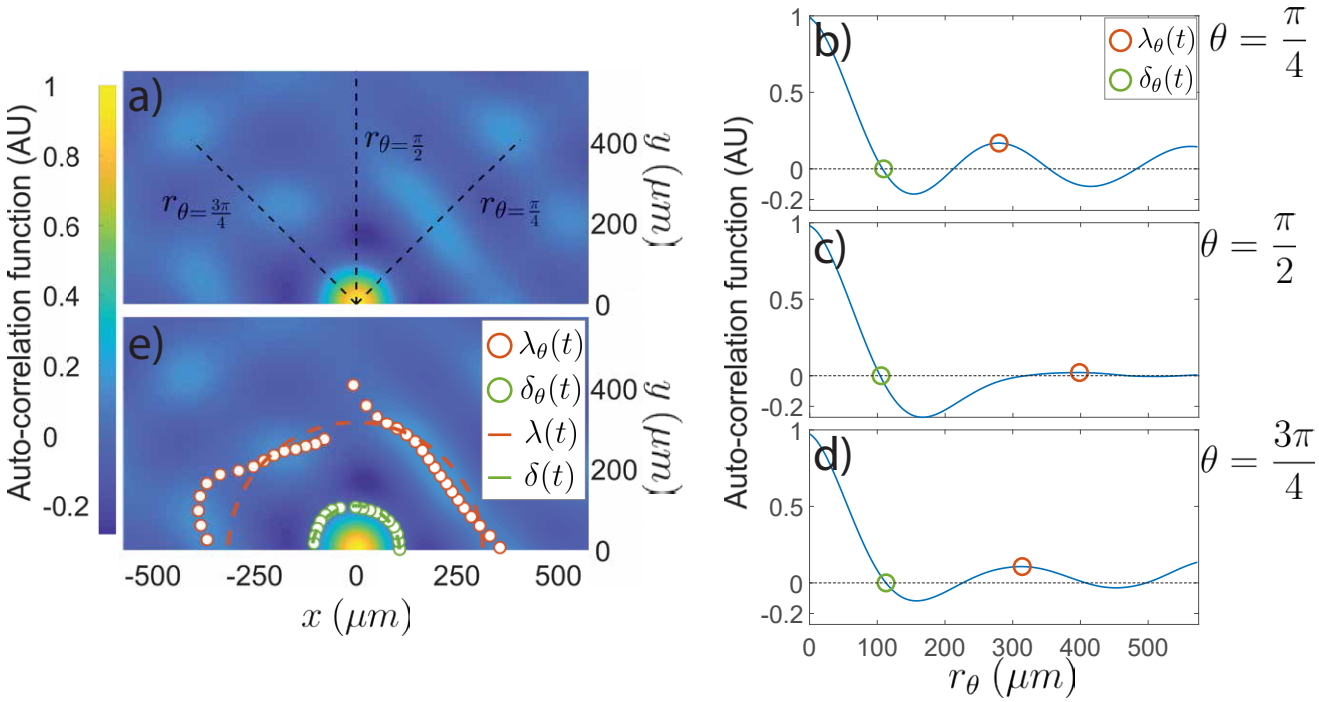


Figure 2.12: a) Two dimensional auto-correlation function inside the reduced zone. Three radii were drawn for three different angles. b-d) Auto-correlation function values through the three cuts shown in figure a) and the respective detection of $\delta_\theta(t)$ and $\lambda_\theta(t)$. e) Detected $\delta_\theta(t)$ and $\lambda_\theta(t)$ in the two dimensional correlation function, shown as white markers with green and orange edges, respectively, and the subsequent calculation of $\delta(t)$ and $\lambda(t)$ represented as the radius of the segmented-lined semi-circle.

# Chapter 3

# Results

## 3.1. General behavior

For each experimental realization, a clean, new chamber was inoculated with a fresh dense suspension of MTB, positioned at the center of the Helmholtz coils setup in the microscope and the magnetic field was turned on while recording with the camera. Several videos of different realizations of the experiment were obtained. Figure 3.1 shows snapshots of some representative examples. Dark and light regions correspond, respectively, to high and low concentrations. A homogeneus magnetic field is applied at $t = 0$. Different rows correspond to different experiments, performed at different experimental conditions, as explained in the caption.

Once the magnetic field is applied, the bacterial suspension responds in a somewhat predictable behavior, as explained next. In absence of an external magnetic field, the homogeneous state does not show any spatial scale or temporal evolution. As soon as the homogeneous magnetic field $\vec{B}$ is applied on the opposite direction of gravity acceleration $\vec{g}$, the image darkens. The reason behind this is not clear, but could be related to an immediate hydrodynamic attraction between bacteria due to the instantaneous alignment that the magnetic field imposes. If the applied magnetic field is removed, the system then goes back to the homogeneous state. Examples of the homogeneous state can be observed in Figs. 3.1 a), e) and i).

If the magnetic field is left to act over the MTB suspension, characteristic spatial patterns appear. Dark spots become visible, differentiating themselves from brighter spots. These dark spots correspond to bacteria accumulation, similar to those shown in figure 1.14, meaning that bacteria start to interact attractively and accumulate in some regions. Examples of this early clustering can be observed in Figs. 3.1 b), f) and j).

As time passes by, dark zones start to get darker and bright zones brighter. Seemingly random distributions and shapes start to organize into larger patterns. Those patterns are stable in time, meaning that apparently the system stops evolving. It is unknown if there is

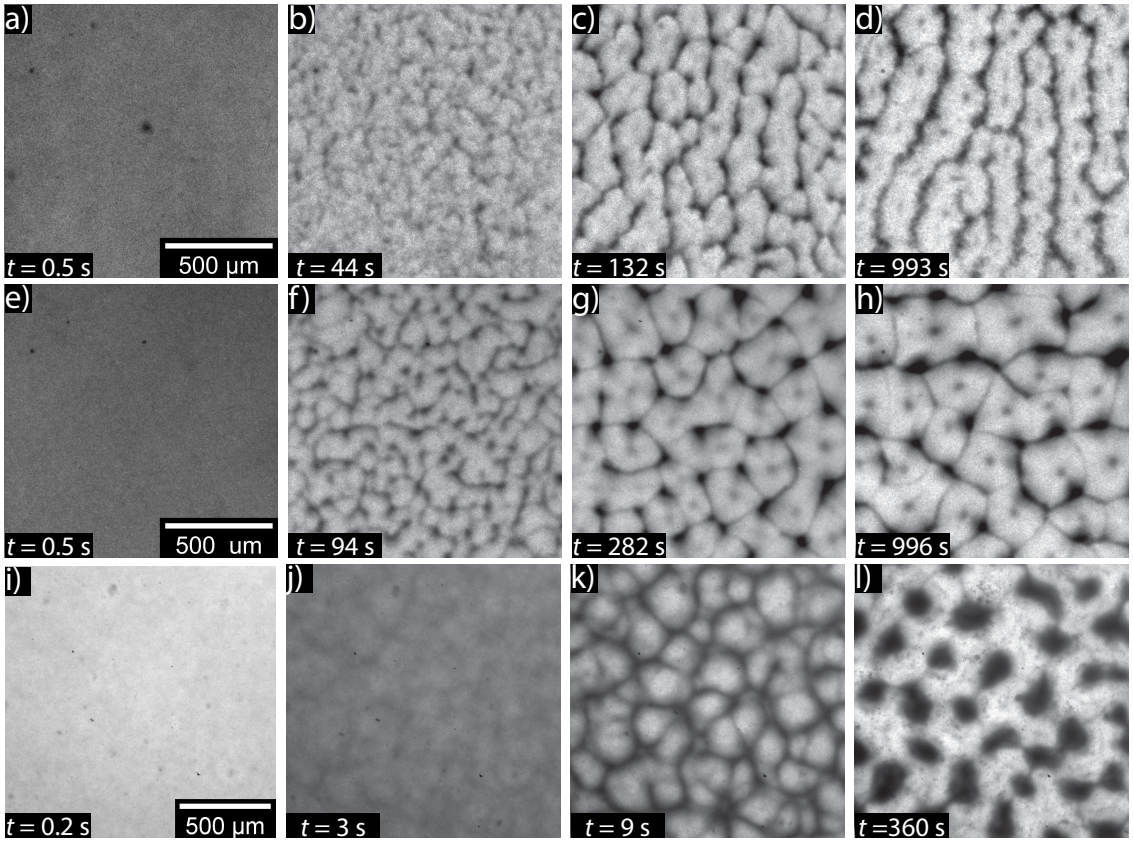


Figure 3.1: Snapshots of three experiments at different times. Figures a-d) correspond to an experiment with OD = 38.9, $h = 50\,\mu\text{m}$, $B_z = 2\,\text{mT}$. e-h) OD = 47.6, $h = 100\,\mu\text{m}$, $B_z = 2.1\,\text{mT}$. i-l) OD = 50.1, $h = 200\,\mu\text{m}$, $B_z = 4.1\,\text{mT}$. These experiments are highlighted in the phase diagram of figure 3.3.

a larger scale temporal evolution, longer than the duration of the videos.

A variety of final patterns were observed, of different shapes and sizes. In general they can be qualitatively classified in three types: clusters (figure 3.1 l)), cells (figure 3.1 h)) and bands (figure 3.1 d)), although in some cases the classification is not clear. Bands can be described as accumulation zones being elongated in one specific direction due to the presence of external flows, which appear uncontrollably, possibly due to the presence of a bubble or to a poor seal of the chamber. There is a clear appearance of an anisotropy in the direction of the flow as it steers the accumulated bacteria. The mechanism is visualized in figure 3.2. Since bands are related to an uncontrolled external parameter, they will not be taken into account in the quantitative analysis. Cells can be recognized as point accumulations, separated between each other by accumulation lines, which sometimes draw pentagons or hexagons around the central points. In the vertexes of these shapes, accumulation points can also be observed. Clusters correspond to point accumulations that seem to be isolated from their neighbors.

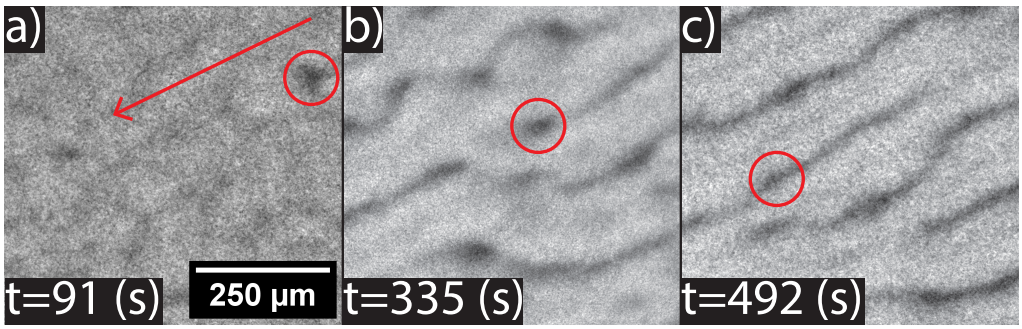


Figure 3.2: Snapshots of an experiment showing the formation of a band from a single cluster. The red arrow points at the direction of the flow, which has a speed of $\sim 1\,\mu\mathrm{m\,s^{-1}}$. The red circles mark an initial cluster that is being dragged by the flow, leaving an elongated streak of bacteria behind.

The experiment has four control parameters: the magnetic field intensity $B_z$, the height $h$ of the chamber, the concentration of bacteria measured by the OD, and the type of cavity (PDMS/glass or glass/glass). A phase diagram for the type of pattern is shown in figure 3.3, with OD in the abscissa, $h$ in the ordinate, and $B_z$ in the color scale. Symbols with a black edge were carried out with the double-side adhesive tape on glass/glass cavities, while the orange edge corresponds to experiments with PDMS/glass cavities. The symbols shape represent the pattern type observed, whether clusters, cells or bands.

In general, for glass/glass cavities, all types of pattern were likely to form. On the contrary, for experiments performed with PDMS/glass cavities, clusters were the only type of pattern. For $h = 200\,\mu\mathrm{m}$, clusters were mainly observed independent on the magnetic field intensity and the type of confinement used, with the exception of one case, where bands were obtained due to the presence of flows. $h = 100 - 110\,\mu\mathrm{m}$ is the case were more cells appeared, in a similar amount as clusters, for different values of OD and $B_z$. For $h = 50\,\mu\mathrm{m}$, experiments were performed mainly for $B_z = 4\,\mathrm{mT}$ and only one with $B_z = 2\,\mathrm{mT}$. Bands were most likely to appear in this case. Clusters formed for OD $> 51$ and two experiments formed cells.

A common feature can be observed in some experiments. Intermediate concentration zones appear between bands in figure 3.1 d) and at the center of the cells in 3.1 h), recognizable by a middle gray value. To explore the difference between high density zones and intermediate density zones, a particle image velocimetry (PIV) measurement was made once the patterns were already settled on an experiment performed with polymer-fabricated Helmholtz coils (see section 2.2.2), in which, fortunately, the focus plane shifted between the bottom and the top plates, allowing us to measure the flow field in both sides but leaving the uncertainty as to which one is the top or the bottom glass. Figure 3.4a) shows a frame of the experiment. The divergence of the velocity field in both planes is shown in figures 3.4b) and c). Positive values of the divergence correspond to source flows, and negative values of the divergence correspond to sink flows. It is observed that high concentrations zones behave as sinks and intermediate concentration zones as sources in one of the plane. This is reversed when the

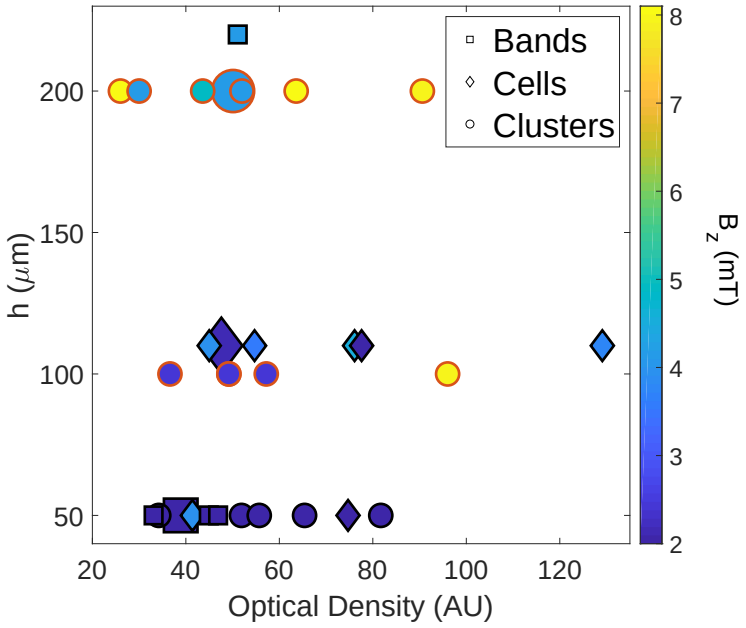


Figure 3.3: Phase diagram of the experiments. Experiments are shown, distributed according to the three main parameters, $h$ in the abscissa, OD in the ordinate, $B_z$ in the color bar and glass/glass (black edges) and PDMS/-glass (orange edges) classification. Also, the type of pattern formed in the quasi stationary state is shown, with squares corresponding to bands (3.1, d)), diamonds corresponding to cells (3.1 h)) and circles corresponding to clusters (3.1, l)). The bigger markers show the location on the phase diagram of the experiments shown in figure 3.1.

plane of view changes to the opposite wall of the cavity.

It has been mentioned that the flows surrounding a bacterial accumulation have the form diagrammed in figure 1.14c) and measured in figure 1.15e), that is, attractive at the sides of the plume and repellent at the rear. With that information, it can be deduced that bacterial cumulus are located at the plane at which accumulation zones behave as a sink. If that is the case, intermediate density zones locate at the opposite wall to that of high density zones. With that in mind, three situations can be considered, identified as segmented lines over the experiment frame in figure 3.5a). On one hand, it is possible that this is caused by SS and NS plumes forming on opposite walls, leading to the interaction between their flows and thus drawing the pattern observed. However, if there is an asymmetry in the population of NS and SS, larger clusters of the dominant population will form in one of the planes and smaller, lighter clusters will form on the opposite one, as is the case in figure 3.4a) and in the bands shown in figure 3.1d). Differences in NS and SS clusters could also be due to the presence of an oxygen gradient that causes bacteria to accumulate preferentially in one of the walls; also, gravity could be the reason behind this, since the magnetosome adds an extra mass to each bacterium, making them slightly denser than the medium. The interaction between clusters formed in opposite walls is diagrammed in figure 3.5b).

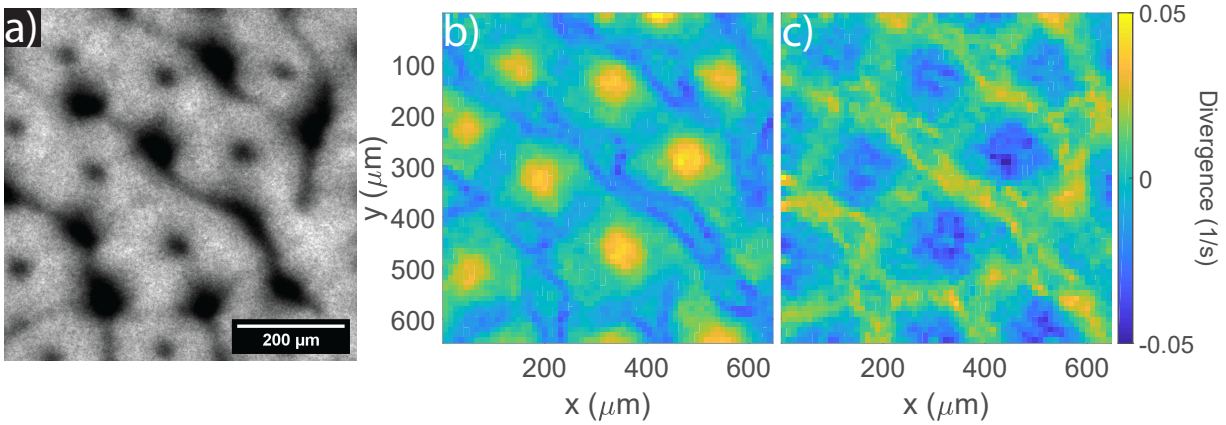


Figure 3.4: A PIV measurement was perform in an experiment inside a glass/glass cavity. a) Cell-like type of pattern in the quasi-stationary state. b) Divergence of the flow field near one glass slide. Intermediate density regions appear as sources and high density regions appear as sinks. d) Divergence of the flow field near the opposite glass slide to that of b). The behavior of the flows is reversed, so that intermediate density regions now appear as sinks and high density regions as sources.

On the other hand, plumes should always collapse in a circular shape seen from above due to hydrodynamic interactions between swimming, pusher type of bacteria, and thus the accumulation lines observed to form around the cells are intriguing. One possibility is that "dead" or non-swimming bacteria which are always present to some degree, are dragged by the flow produced by the plumes and accumulate at the stagnation lines of the flow, as diagramed in figure 3.5c). These lines seem to appear only at one of the walls, which would indicate that, for the final pattern to be in the form of cells, both an asymmetry in the NS/SS cluster size and an appreciable amount of non-swimming bacteria have to exist.

Finally, clusters formed in the same wall can interact without leaving accumulation lines between them, as it is diagrammed in figure 3.5d). In this case, the same flow pattern is formed, showing that it is not necessary to have two populations of MTB (NS and SS) for the formation of these patterns.

## 3.2. Characteristic temporal scales in the formation of the patterns

As explained in section 2.3, the auto-correlation function computed from the recorded images of the experiment constitutes a useful tool to extract information regarding a characteristic length in a given periodic structure. When analyzed over time, results such as the ones shown in figure 3.6 can be obtained, where the two dimensional auto-correlation

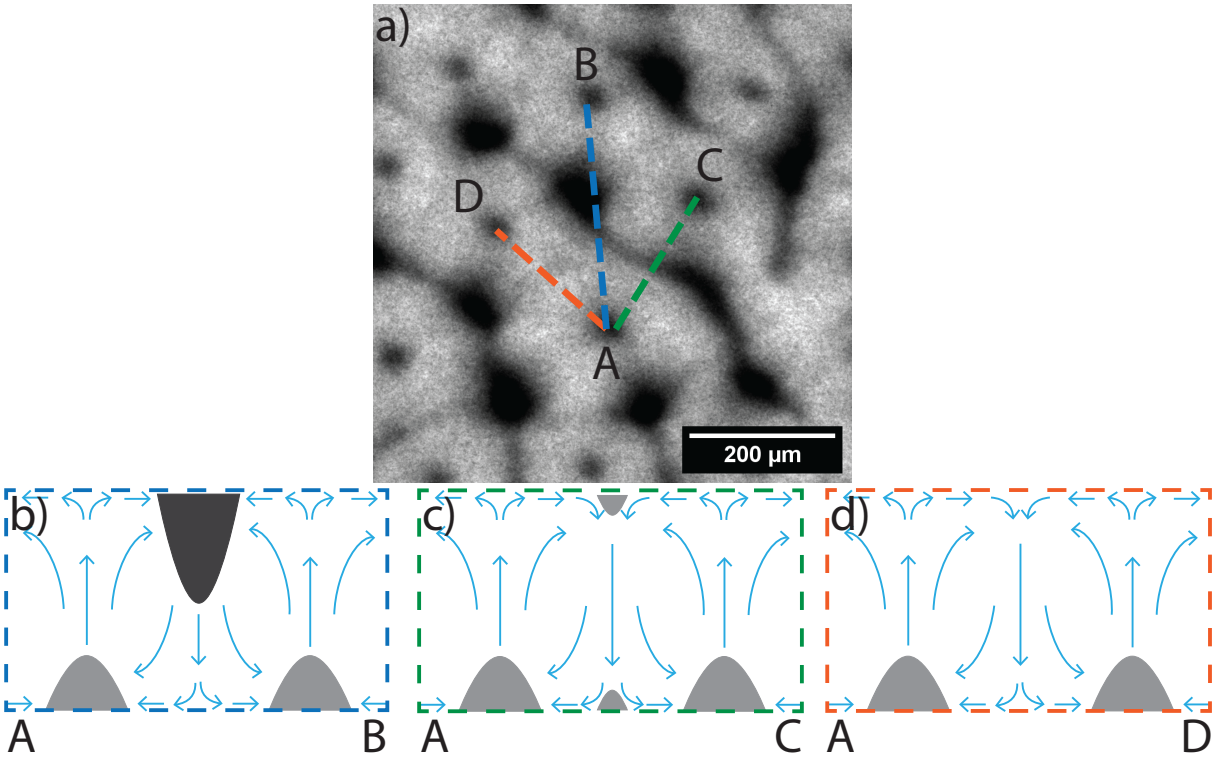


Figure 3.5: Interaction between accumulation zones. a) Experimental image with cell-like type of patterns. The segmented lines $\overline{AB}$, $\overline{AC}$ and $\overline{AD}$ correspond to transverse cuts that indicate three types of interactions. b) Diagram of $\overline{AB}$ transverse cut, showing the interaction between asymmetrical NS/SS clusters formed at different walls. c) Diagram of $\overline{AC}$ transverse cut, showing the interaction between clusters formed at the same wall leading to the accumulation of non-swimming bacteria at the stagnation lines. d) Diagram of $\overline{AD}$ transverse cut, showing the interaction between clusters formed at the same wall, where there is no accumulation at the stagnation lines.

function in figures 3.6 a), b) and c), show the appearance of the zeros and local maxima around the center. This is evidence of pattern formation in the experiments.

A mean of all zeros and a weighted mean of all local maxima was computed for each frame, giving a value for the characteristic size of the structures $\delta_t$ and a characteristic distance $\lambda_t$ as it was previously explained in section 2.3. Figures 3.6a-c) show the location of some $\delta_i$ and $\lambda_i$ as white circles with green and orange edges, respectively, in the two dimensional auto-correlation function, as well as the computed $\delta_t$ and $\lambda_t$ as the radius of the semi-circle drawn with a segmented green and orange line, respectively, for three different times of the experiment shown in figures 3.1e-h). Figures 3.6 d) and e) show the time evolution, $\delta(t)$ and $\lambda(t)$ for the same experiment.

By looking at figures 3.6 d and e), it is possible to identify two regimes in the time evolution of $\lambda$ and $\delta$. The early stage is characterized by a rapid increase in their value, related to the passing from a homogeneous state to an ordered state. After a specific time, the in-

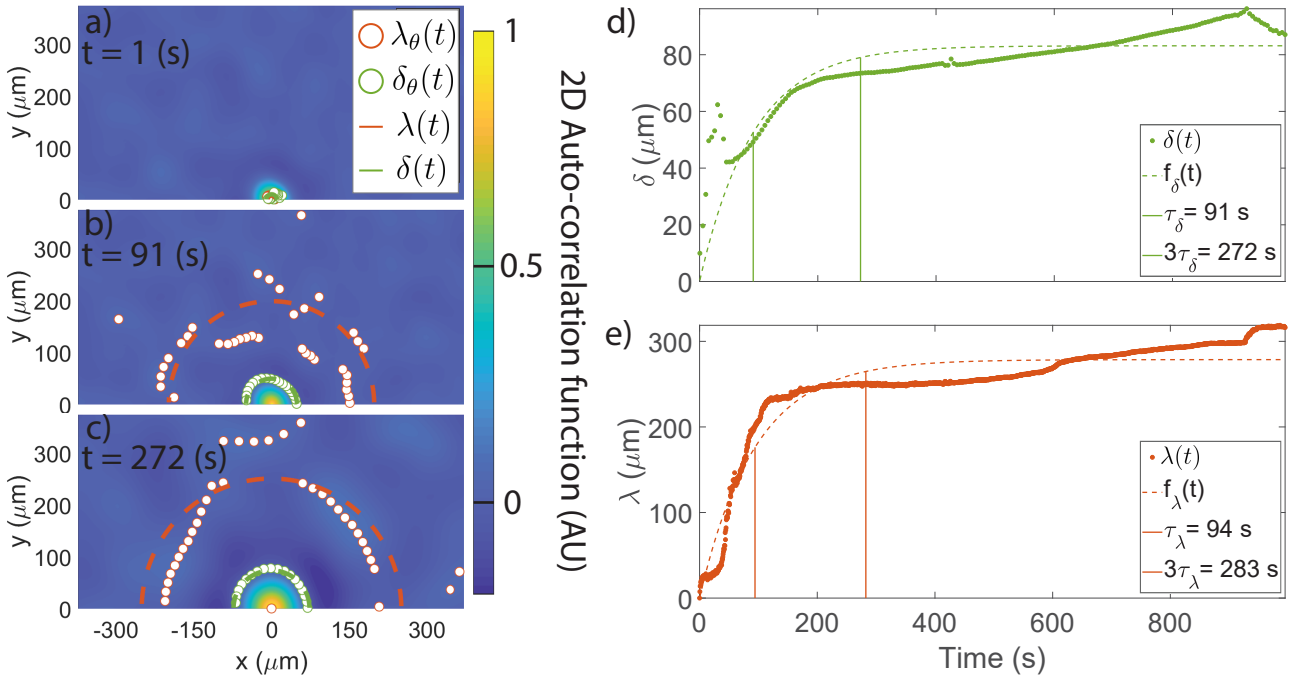


Figure 3.6: Time evolution of the auto-correlation function. Figures a-c) show the two dimensional auto-correlation function for $t$ =1 s, $t = \tau_\delta = 91$ s and $t = 3\tau_\delta = 272$ s respectively. The white markers with green edges mark the position of some $\delta_i$ and the white markers with orange edges mark the position of some $\lambda_i$. The segmented lines illustrate the computed $\delta_t$ and $\lambda_t$ for the respective frame. Figures d) and e) show the temporal evolution of $\delta_t$ and $\lambda_t$, as well as a curve given by equation 3.1. The characteristic times $\tau_{\delta,\lambda}$ are highlighted as well as $3\tau_{\delta,\lambda}$.

creasing of characteristic distances slows down, reaching a quasi-stationary state.

In order to compute characteristic times, $\tau_{\delta,\lambda}$, we looked at the shape of $\lambda(t)$ and $\delta(t)$ and fitted a function of the form

$$f_{\delta,\lambda}(t) = A_{\delta,\lambda}(1 - e^{\frac{-t}{\tau_{\delta,\lambda}}}). \tag{3.1}$$

Note that $f_{\delta,\lambda}(t = 0) = 0$ and $\lim_{t\to\infty} f_{\delta,\lambda}(t) = A_{\delta,\lambda}$, meaning that the function approaches asymptotically a constant value, different to the observed behavior in the experiments, which reaches a quasi-stationary state. Nevertheless, the evolution in the quasi-stationary state is so slow, that $f_{\delta,\lambda}$ still is a good fit. $\tau_\delta$ corresponds to the characteristic time of cluster formation, while $\tau_\lambda$ corresponds to the characteristic time of pattern establishment, such that at $t = \tau_{\delta,\lambda}$ the system will have reached a 63 % of evolution towards the quasi-stationary state, and at $t = 3\tau_{\delta,\lambda}$ a 95 %.

The values of $\tau_{\delta,\lambda}$ were determined for every experiment, and their dependence on the experimental parameters were studied. Figure 3.7 shows the dependence of $\tau_\delta$ on the density of bacteria for $h = 50\,\mu$m, $h =$ 100-110 $\mu$m and $h = 200\,\mu$m. The intensity of the magnetic field is shown in color.

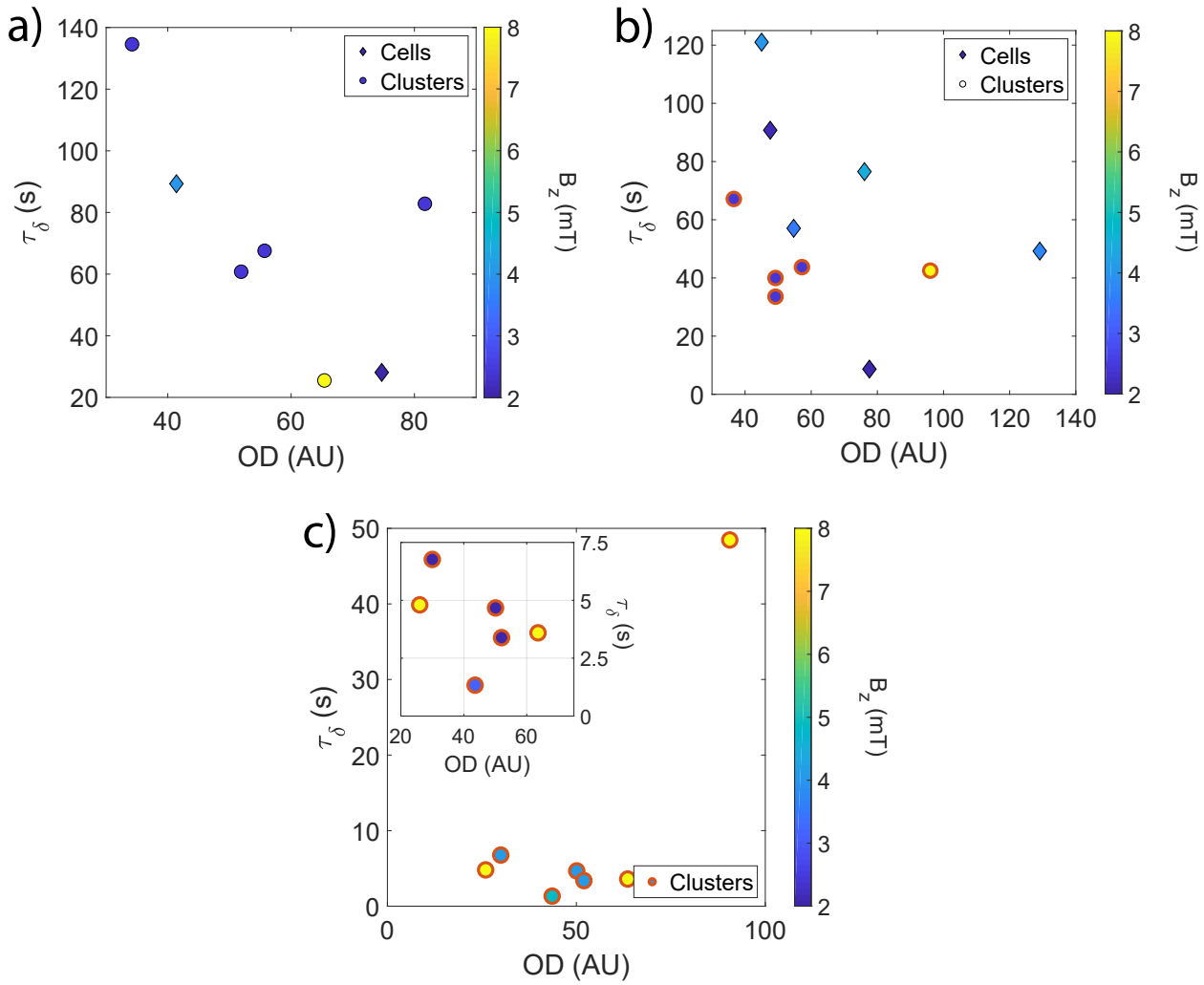


Figure 3.7: Relationship between the characteristic time for $\tau_\delta$ and the density, for a) $h = 50\,\mu$m, b) $h = 100$-$110\,\mu$m and c) $h = 200\,\mu$m. The inset corresponds to a zoom of the smaller $\tau_\delta$ points.

For $h = 50\,\mu$m, as density increases, $\tau_\delta$ decreases, with the exception of one point. No dependence is observed on the magnetic field intensity, nor on the type of pattern formed, since clusters or cells can have low or high characteristic times. Overall, for $h = 100 - 110\,\mu$m, the behavior is similar to that of $h = 50\,\mu$m, but with higher dispersion. Again, no dependence on the magnetic field is observed. Regarding the type of pattern, clusters seem to have lower values of $\tau_\delta$. It is also visible that clusters are more likely to appear when there is a higher oxygen presence, since no cells where observed in the PDMS/glass chambers. For $h = 200\,\mu$m, the values of $\tau_\delta$ tend to be lower than in the cases for $h = 100 - 110\,\mu$m, with values as small as 1.3 s for one experiment. This is evidence of a faster dynamic that is not present in the other experiments. Aside of the highest density point, $\tau_\delta$ shows a decreasing tendency. An abrupt change occurs when the OD value is sufficiently high, showing an elevated value for the higher density point exhibited in the figure.

Figure 3.8 shows the characteristic time scale for the establishment of the pattern, $\tau_\lambda$ as a function of the density and the magnetic field intensity.

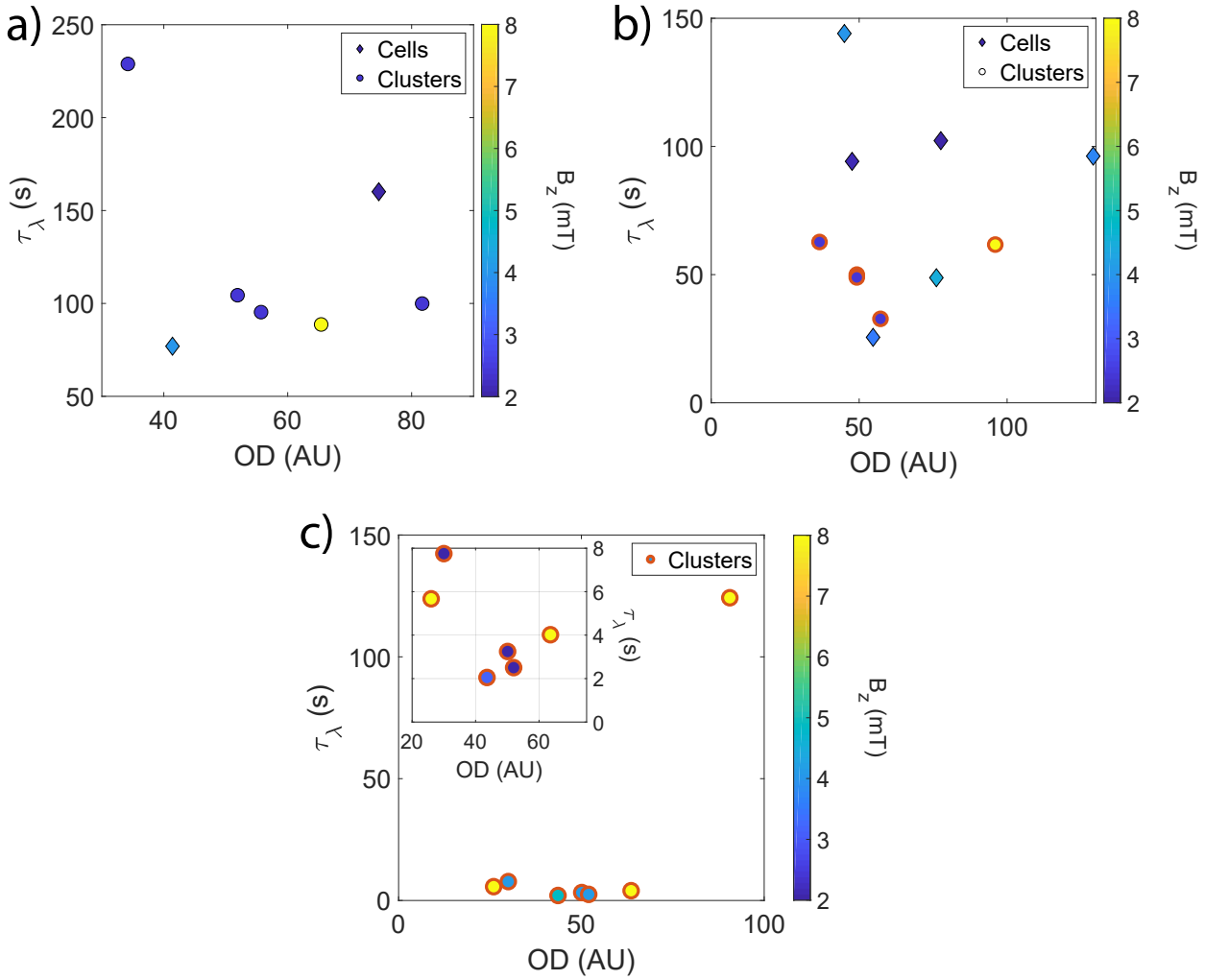


Figure 3.8: Relationship between the characteristic time $\tau_\lambda$ and the density, for a) $h = 50\,\mu$m, b) $h = 100$-$110\,\mu$m and c) $h = 200\,\mu$m. The inset corresponds to a zoom of the smaller $\tau_\lambda$ points.

For $h = 50\,\mu$m, $\tau_\lambda$ seems to have a decreasing behavior, specially for clusters, starting at a high value of $\tau_\lambda$ for the lower density point, and decreasing as density increases. The dispersion is a contribution of cell-like patterns. Again, no dependence on the magnetic field intensity is observed.

For $h = 100\,\mu$m, $\tau_\lambda$ seems to have a lot of dispersion. The weak tendency observed for $\tau_\delta$ in this chamber height is lost. Again, no dependency on the magnetic field intensity is observed. In general, clusters seem to form faster than cells, except for the case of two experimental realizations where cells were formed with time scales of 50 s or below.

For $h = 200\,\mu m$, the behavior of $\tau_\lambda$ is almost identical to $\tau_\delta$: with exception of the high density point, there appears to be a decreasing behavior and patterns form very quickly.

In general, the most consistent tendency seems to be that the time of formation of patterns, decreases as density increases. This is supported by simulations made in [Théry et al., 2020], but the dispersion present in our measurements makes it hard to extract strong conclusions.

Figures 3.9 a) and b) show the relationship between the characteristic times and the confinement height $h$.

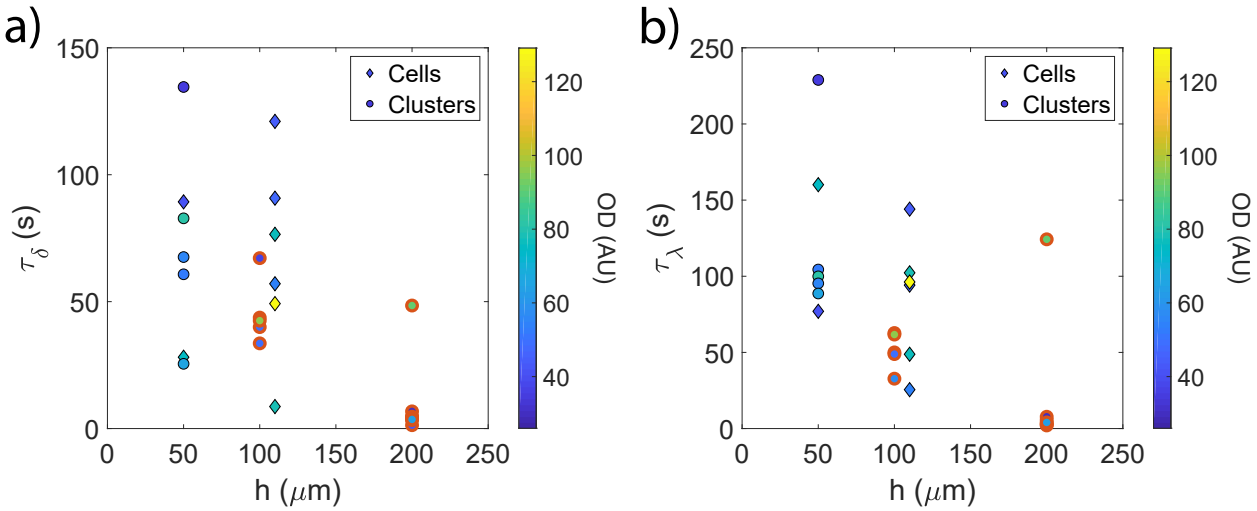


Figure 3.9: Dependence of the characteristic times $\tau_\delta$ and $\tau_\lambda$ on the confinement size $h$.

Although a lot of dispersion is present, one can say that for higher values of $h$, both characteristic times decrease, especially for $h = 200\,\mu m$. This is specially evident if only the data points obtained with high oxygenation are considered.

Figure 3.10 shows the relationship between $\tau_\delta$ and $\tau_\lambda$. The dispersion suggests that both times are not correlated, meaning that high density zones form independently of the global pattern. Bacterial clusters form with a characteristic time $\tau_\delta$, the general periodicity forms with a characteristic time $\tau_\lambda$, and both phenomena occur in parallel but independent of each other. Nevertheless, a grater number of points seem to be located above the $f(x) = x$ curve, indicating that the structures in general form before the patterns settle.

If only experiments performed with a PDMS/glass cavity are considered, aside of an outlier point, the points are located near the $f(x) = x$ curve. Consistently with what is observed in figure 3.9, oxygenation seems to diminish dispersion.

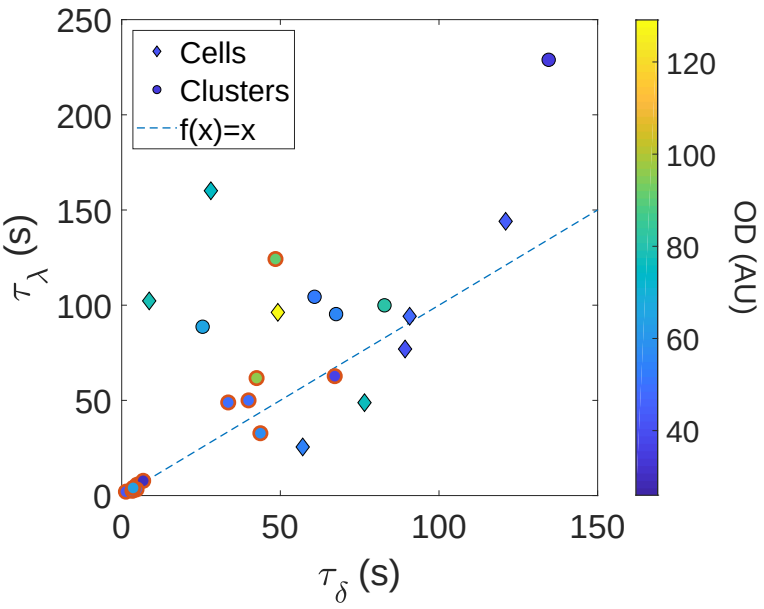


Figure 3.10: Relationship between the $\tau_\lambda$ and $\tau_\delta$. The segmented line corresponds to the function $f(x) = x$ that works as a reference line. Points located above that line indicate that the structures formed faster than the patterns settled. Below that line, patterns established faster than the structures formed.

## 3.3. Characteristic length scales in the quasi-stationary state

For each experiment, the average value for the small structure size, $\delta_c$, and for the spatial periodicity, $\lambda_c$, were computed by averaging each parameter between $3\tau_\delta$ or $3\tau_\lambda$, and the end of the experiment, respectively. Those values, $\delta_c$ and $\lambda_c$, will correspond to characteristic sizes and separation between structures respectively. Figure 3.11 illustrates this for one example of cells and one of clusters.

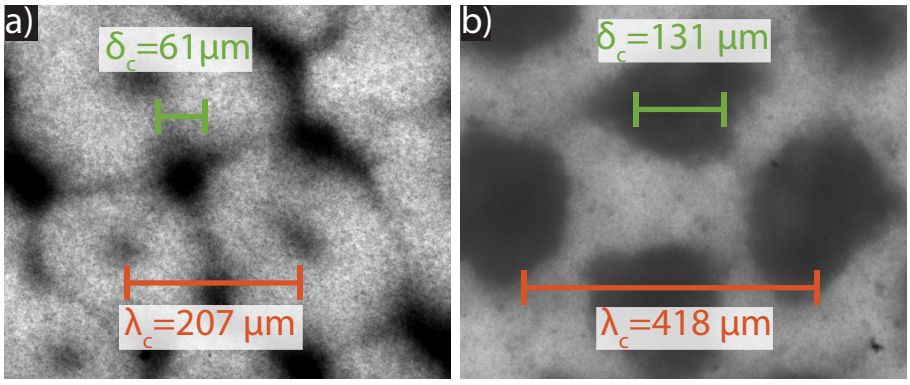


Figure 3.11: Measurements of $\delta_c$ and $\lambda_c$ illustrated on screen-shots of two different experiments.

Figure 3.12 shows the behavior of $\delta_c$ as a function of bacterial density and magnetic field intensities.

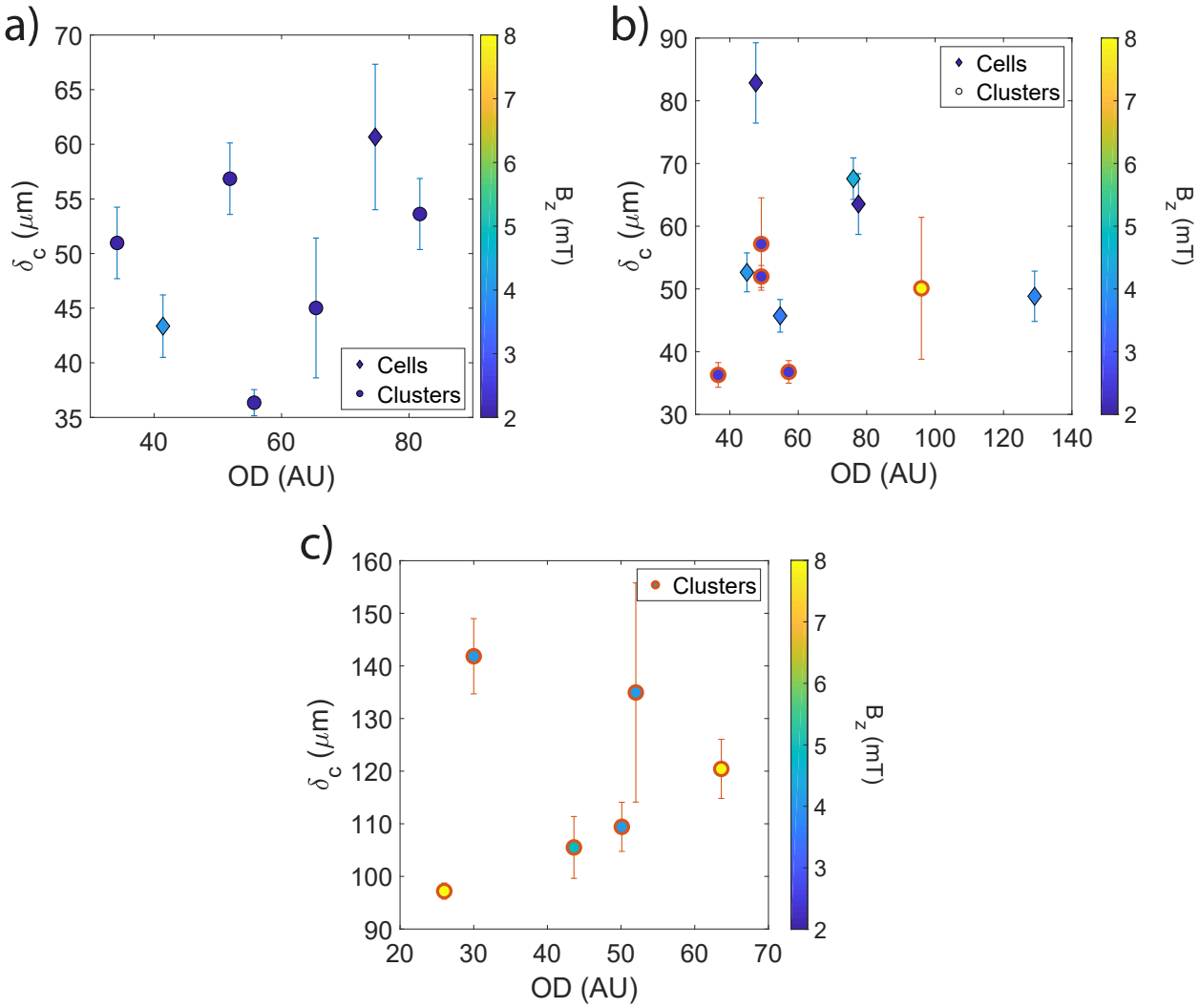


Figure 3.12: Relationship between the characteristic size $\delta_c$ and the density, for a) $h = 50\,\mu$m, b) $h =$ 100-110 µm and c) $h = 200\,\mu$m.

For the three different values of $h$, a high level of dispersion is observed, regardless on the type of pattern. But, as $h$ increases, higher values of $\delta_c$ are obtained.

Figure 3.13 shows the behavior of $\lambda_c$ as a function of the density and the magnetic field intensity.

The behavior of $\lambda_c$ is very similar to that of $\delta_c$. No significant differences are observable, regardless of the height. Just as in the case of $\delta_c$, the increasing of $\lambda_c$ with increasing height is noticeable.

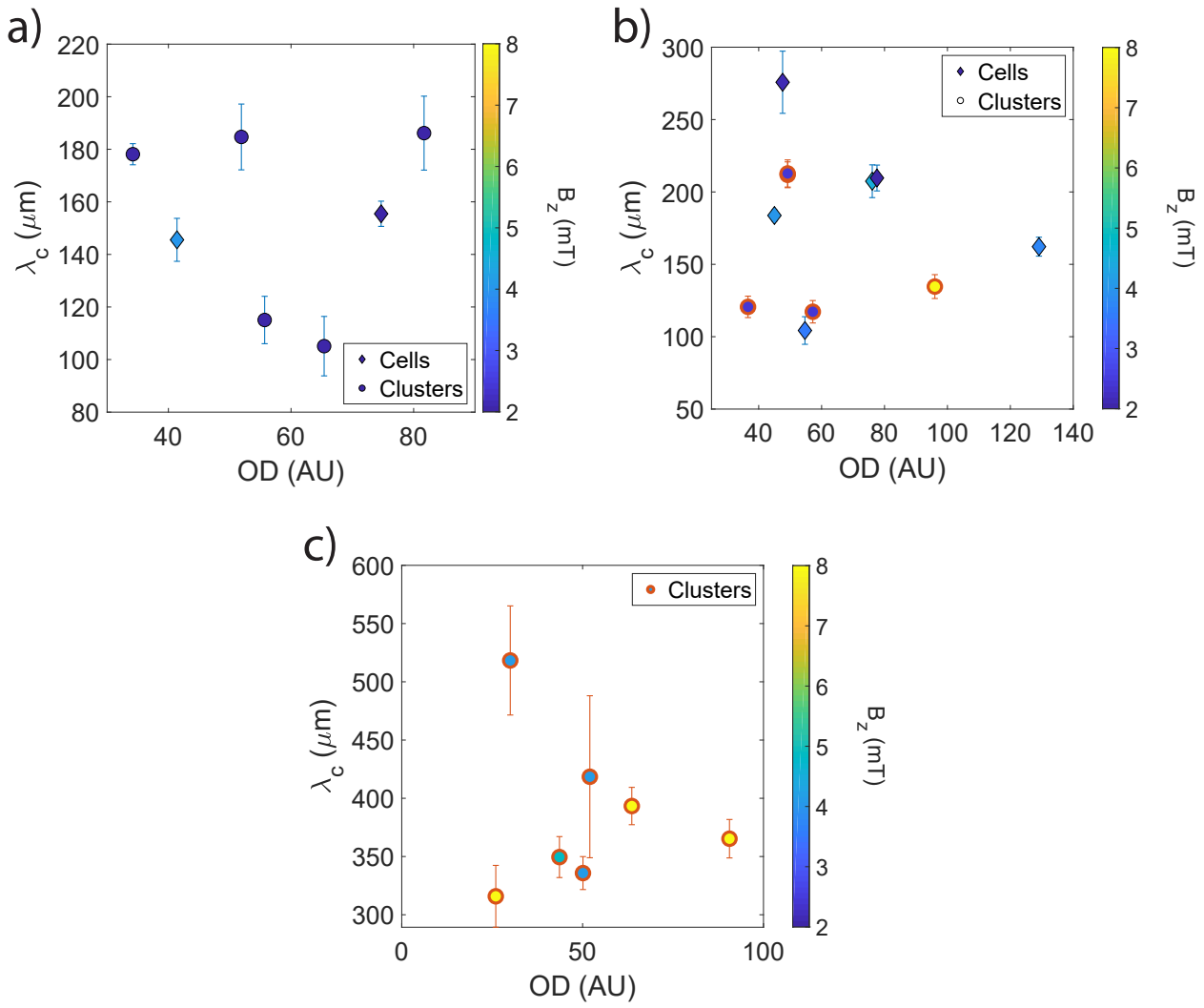


Figure 3.13: Relationship between the characteristic size $\lambda_c$ and the density, for a) $h = 50\,\mu$m, b) $h = 100$-$110\,\mu$m and c) $h = 200\,\mu$m.

Figure 3.14 shows the dependence of $\delta_c$ and $\lambda_c$ with the confinement height $h$. Here it is evident that at higher values of $h$, the characteristic sizes are higher. In both cases, linear fits are applied and compared with the function $f(x) = x$, ie. the case in which the smaller structures or the spatial periodicity coincides with the height of the confinement. For $\delta_c$, the slope of the linear fit is lower than 1, unlike for $\lambda_c$, which has a higher slope. This contradicts the findings of Ref. [Théry et al., 2020], where the authors find that plumes in long capillaries of square cross section (shown in figure 1.15) form in a periodic pattern with wavelength equal to the side of the capillary. In figure 3.14 b) the value of $\lambda_c$ is bounded by below by the chamber height $h$.

In figure 3.15, the dependence of the characteristic times as a function of the characteristic sizes is shown, displaying also the height $h$ in the colorbar. This in order to observe if the time that takes to the structure to form is related with the size itself. It is tempting to say

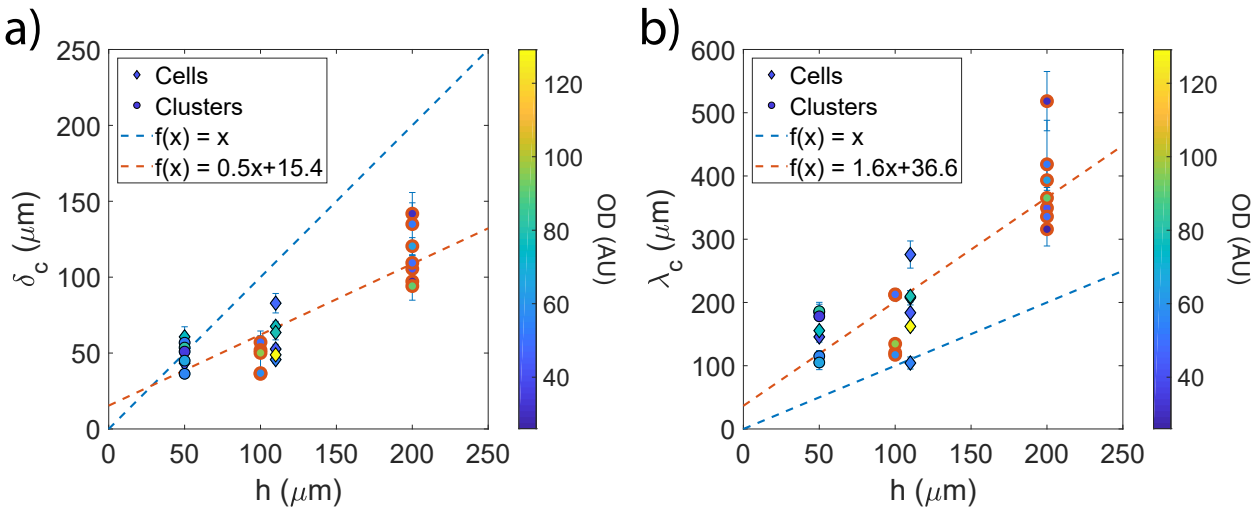


Figure 3.14: Dependence of the characteristic distances $\delta_c$ and $\lambda_c$ on the confinement size $h$.

that larger structures take less time to form, but this apparent tendency is dominated by the data points with $h = 200\,\mu$m, which have very fast dynamics compared to the other cases. Considering that, the rest of the points in the graphics can be seen as highly disperse.

Again, if only PDMS/glass experiments are considered, the general dispersion is diminished.

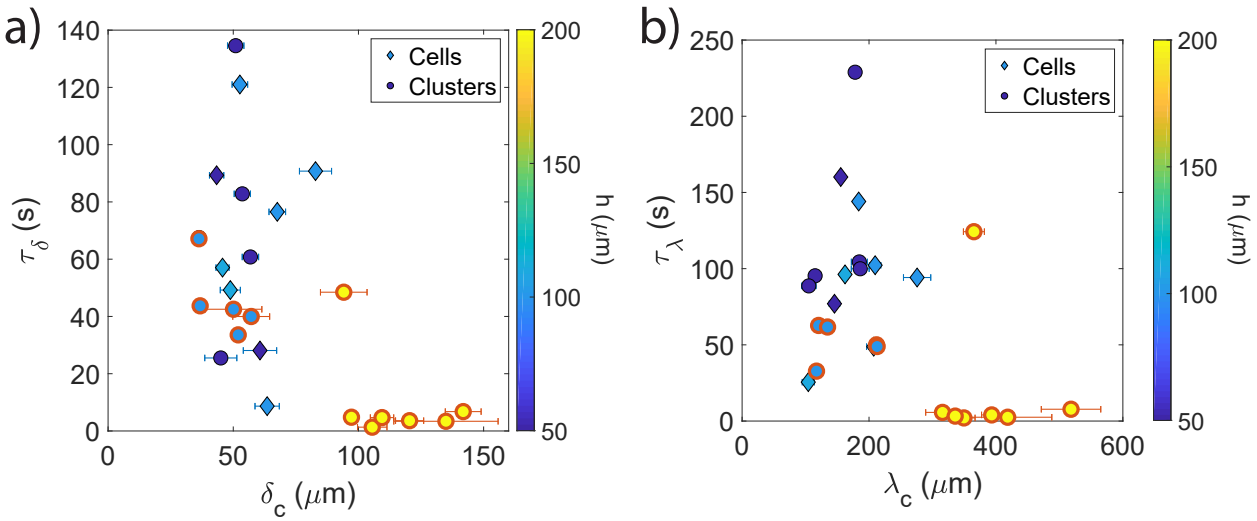


Figure 3.15: Dependence of the characteristic times $\tau_\delta$ and $\tau_\lambda$ on the characteristic distances $\delta_c$ and $\lambda_c$ respectively.

Figure 3.16 shows the behavior of $\lambda_c$ as a function of $\delta_c$. Here, a consistent conduct is observable. A higher size of the structure presents a higher separation. A fit of the form

$f(x) = ax$, with $a = 3.3$, is shown.

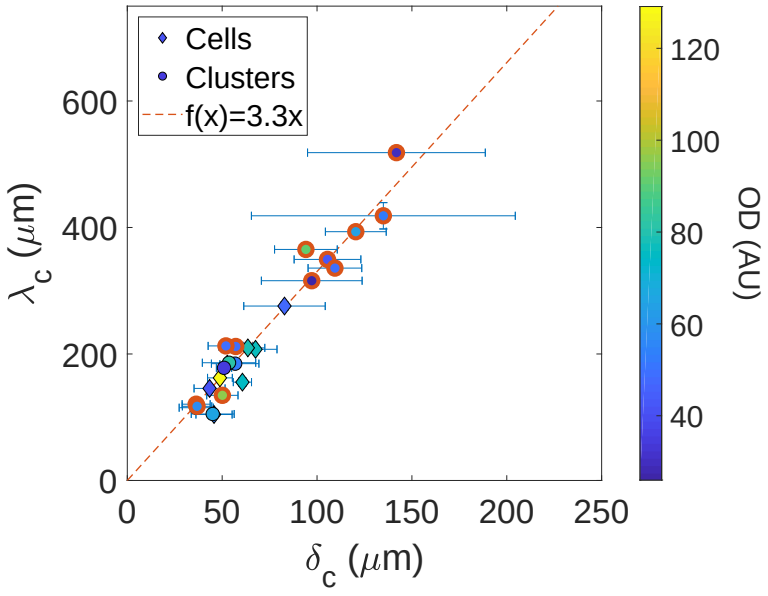


Figure 3.16: Relationship between the characteristic separation $\lambda_c$ with the characteristic size $\delta_c$. The segmented line shows a fit of the form $f(x) = ax$.

# Chapter 4

# Conclusions and perspectives

In this thesis, we observed the collective behavior of high-density suspensions of biased magnetic microswimmers *Magnetospirillum Gryphiswaldense* under confinement. A qualitative description of the temporal evolution of the system, and of the variety of final pattern observed was given. The two-dimensional auto-correlation function of the recorded images was calculated in order to extract quantitative values, that were observed and compared with the experiment control parameters: density, confinement height, magnetic field intensity and oxygenation.

Of all the control parameters, the one that has the largest effect on the patterns is the height of confinement $h$ where a tendency is observed, supported by the results obtained in [Théry et al., 2020]. A difference between the two results is in regards of the slope of the dependence. For the separation of the plumes, they suggest a $f(x) = ax$ with $a = 1$ dependence. In contrast, we obtained a dependence with $a = 1.6$. This difference can be explained by the addition of an extra dimension to the experiment.

Oxygenation also seems to have a large impact in the overall shape and dynamic of the patterns. It was observed that for PDMS/glass cavities (where oxygen is allowed to diffuse inside the cavity through the PDMS) clusters are more likely to form, with the exception of one experiment that showed cell formation. A fast dynamics was observed for PDMS/glass cavities with confinement heights $h = 200\,\mu\text{m}$ which was visible in the lower $\tau_\delta$ and $\tau_\lambda$ values, but since this is not consistently observed for other values of $h$ it is not clear which parameter is responsible of this. It was explained in section 1.1.3 that aerotaxis may be the dominant tactic behavior in MTB and, since oxygen has to diffuse from one wall to the other, passing through the bacterial bulk, an interplay between $h$ and oxygen concentration gradients could be triggering this fast dynamics.

An unexpected dispersion was observed when looking at the dependence of the characteristic times and length scales on density. The proximity at which bacteria interact with each other should play a major role in the measurement of characteristic times or sizes. The

results obtained show no tendencies, aside of those shown in figures 3.7 a), b) and c). This is rapidly contradicted by the results shown in figures 3.8. An unexplored effect regarding the experiment protocols, could be behind this, specifically in the densification of the suspension (section 2.1.3), where the centrifugation process and the re-suspension of the pellet could potentially harm a large population of bacteria, leaving an uncontrolled number of immotile MTB. It is suggested that, when recording videos, a measurement of the motility of bacteria (post densification) should be made, measuring both mean velocity and motile/immotile number of bacteria ratio. Together with the density of bacteria, this could help explain the general dispersion of the data.

For the magnetic field intensity, it has been found that there is no strong dependence. This is expected since the values of the magnetic field in the experiments exceed for almost two orders of magnitude that of the earth, meaning that, if $B_z = 2$ or $8\,\mathrm{mT}$, it still is too intense for MTB. Nevertheless, measurements of the magnetic moment of magnetotactic bacteria [Rosenblatt et al., 1982] and of its rotational diffusion as a function of the external magnetic field applied [Rosenblatt et al., 1985, Nadkarni et al., 2013, Zahn et al., 2017], can be used in computational simulations in order to test this assumption.

It was observed that bands can be obtained in the quasi-stationary state, resulting from unwanted external flows (figure 3.2). We think that the same patterns can be obtained by tilting the angle of the magnetic field, giving it a component in the $xy$ plane. This could be achieved by fabricating two Helmholtz coils, perpendicular to each other and mounting them in the microscope. By changing the current that passes through the coils, the angle of the magnetic field respective to the $z$-axis can be tuned and used as an additional parameter.

An asymmetry regarding bacteria accumulation in the northern/southern wall was observed (figure 3.4). It was said that magneto-bioconvection is a novel type of bioconvection, since external forces are absent in the work performed by Thery et al. ([Théry et al., 2020]). Nevertheless, in the experiments explained in this thesis, the movement of bacteria is performed either parallel or anti-parallel to the direction of gravity. This could induce another variable to the experiment, regarding the density of a bacterial cell, which thanks to the magnetosome, is thought to be denser than other bacteria that are already denser than water. This can be tested by performing the same experiment, but changing the density of the medium so it can get close to (or higher than) the density of MTB (similar to what was done in [Hosoya et al., 2010]). The results obtained can help us understand the influence of gravity in magneto-bioconvection patterns of MTB.

Another hypothesis regarding this asymmetry is that it is induced by an imbalance between the populations of NS and SS. With the objective of confirming this, exploratory experiments inside a micro-channel were performed (figure 4.1). The results obtained are qualitatively consistent with a larger population of SS than of NS, where a greater accumulation on the

southern magnetic pole of the cavity is observed. Nevertheless, recent experiments similar to the ones performed in this thesis but with magnetic fields oriented parallel or anti-parallel to the direction of gravity, the larger accumulation at the south pole is not always observed, showing also, sometimes, a greater northern pole accumulation. This suggests that imbalances in the population of NS and SS do occur, but that they can occur randomly, favoring one or the other population. Due to the behavior around variable oxygen concentrations [Popp et al., 2014], this experiments have to be performed with a high control of air diffusion inside the cavity.

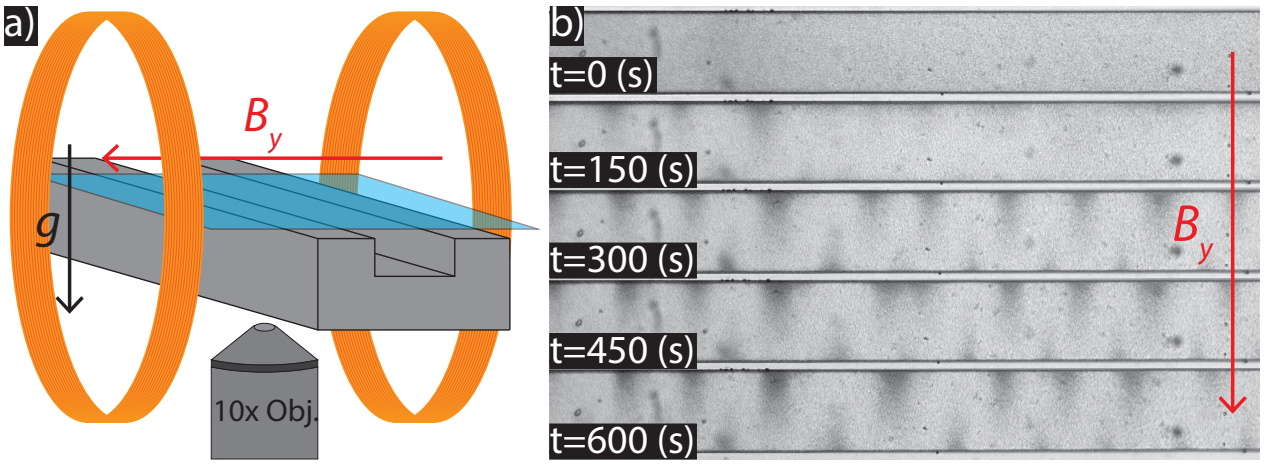


Figure 4.1: Experiment showing the formation of plumes on both sides of a horizontal micro-channel (gravity perpendicular to the observation plane). a) A dense suspension of MTB is inoculated inside a PDMS micro-channel of square cross section and sealed with a glass slide. A magnetic field is applied in the plane perpendicular to gravity at time $t = 0\,\mathrm{s}$. b) From the time the magnetic field is applied, plume formation begins to occur. North pole plumes and south pole plumes begin to intersperse each other. A noticeable asymmetry can be observed, with a higher number of bacteria located at the southern magnetic pole, reflected in the larger size of the plumes. Experiment images courtesy of Pamela Muñoz.

Both behaviors explained above, may suggest that an interplay between gravity and polarity asymmetry could play a role into the spatial differences in the lower-upper walls of the cavity.

The type of cavity with which the experiments were performed, also seems to affect the dynamics. For experiments performed with PDMS/glass cavities, only clusters were formed. Also, by looking at figures 3.9, 3.10 and 3.15, it can be noticed that the source of dispersion are mostly glass/glass experiments, leading to PDMS/glass cavities to have a more consistent behavior.

By being able to weight the gravity and polarity influences, as well as understanding the effects of a tilted magnetic field, a higher control over the final patterns geometry could be

obtained, making this experimental setup a good environment for the study of pattern formation thanks to the broad variety of patterns that can be obtained.

# Bibliography


[Aranson, 2013] Aranson, I. S. (2013). Active colloids. *Physics-Uspekhi*, 56(1):79.

[Armitage, 2001] Armitage, J. P. (2001). Bacterial taxis. *e LS*.

[Arnold and Pahl, 1974] Arnold, G. and Pahl, P. (1974). Some aspects of social behaviour in domestic sheep. *Animal Behaviour*, 22(3):592–600.

[Bazylinski and Frankel, 2004] Bazylinski, D. A. and Frankel, R. B. (2004). Magnetosome formation in prokaryotes. *Nature Reviews Microbiology*, 2(3):217–230.

[Bees and Hill, 1997] Bees, M. and Hill, N. (1997). Wavelengths of bioconvection patterns. *The Journal of Experimental Biology*, 200(10):1515–1526.

[Bees and Croze, 2014] Bees, M. A. and Croze, O. A. (2014). Mathematics for streamlined biofuel production from unicellular algae. *Biofuels*, 5(1):53–65.

[Berg, 2004] Berg, H. C. (2004). *E. coli in Motion*. Springer.

[Berg and Brown, 1972] Berg, H. C. and Brown, D. A. (1972). Chemotaxis in escherichia coli analysed by three-dimensional tracking. *Nature*, 239(5374):500–504.

[Blakemore, 1975] Blakemore, R. (1975). Magnetotactic bacteria. *Science*, 190(4212):377–379.

[Blakemore et al., 1980] Blakemore, R. P., Frankel, R. B., and Kalmijn, A. J. (1980). South-seeking magnetotactic bacteria in the southern hemisphere. *Nature*, 286(5771):384–385.

[Camazine et al., 2001] Camazine, S., Deneubourg, J.-L., Franks, N. R., Sneyd, J., Theraula, G., and Bonabeau, E. (2001). *Self-Organization in Biological Systems*. Princeton University Press, Princeton.

[Cavagna et al., 2010] Cavagna, A., Cimarelli, A., Giardina, I., Parisi, G., Santagati, R., Stefanini, F., and Viale, M. (2010). Scale-free correlations in starling flocks. *Proceedings of the National Academy of Sciences*, 107(26):11865–11870.

[Chaté et al., 2008] Chaté, H., Ginelli, F., Grégoire, G., and Raynaud, F. (2008). Collective motion of self-propelled particles interacting without cohesion. *Physical Review E*, 77(4):046113.

[Chaté and Mahault, 2019] Chaté, H. and Mahault, B. (2019). Dry, aligning, dilute, active matter: A synthetic and self-contained overview. *arXiv preprint arXiv:1906.05542*.

[Childress et al., 1975] Childress, S., Levandowsky, M., and Spiegel, E. (1975). Pattern formation in a suspension of swimming microorganisms: equations and stability theory. *Journal of Fluid Mechanics*, 69(3):591–613.

[Chwang and Wu, 1975] Chwang, A. T. and Wu, T. Y.-T. (1975). Hydromechanics of low-reynolds-number flow. part 2. singularity method for stokes flows. *Journal of Fluid mechanics*, 67(4):787–815.

[Czirók et al., 2001] Czirók, A., Matsushita, M., and Vicsek, T. (2001). Theory of periodic swarming of bacteria: Application to proteus mirabilis. *Physical Review E*, 63(3):031915.

[Foster and Smyth, 1980] Foster, K. W. and Smyth, R. D. (1980). Light antennas in phototactic algae. *Microbiological reviews*, 44(4):572–630.

[Goldstein, 2015] Goldstein, R. E. (2015). Green algae as model organisms for biological fluid dynamics. *Annual review of fluid mechanics*, 47:343–375.

[Gordon, 2019] Gordon, D. M. (2019). The ecology of collective behavior in ants. *Annual review of entomology*, 64:35–50.

[Guyon et al., 2015] Guyon, E., Hulin, J. P., Petit, L., and Mitescu, C. D. (2015). *Physical hydrodynamics*. Oxford university press.

[Hancock, 1953] Hancock, G. (1953). The self-propulsion of microscopic organisms through liquids. *Proceedings of the Royal Society of London. Series A. Mathematical and Physical Sciences*, 217(1128):96–121.

[Hill et al., 1989] Hill, N., Pedley, T., and Kessler, J. O. (1989). Growth of bioconvection patterns in a suspension of gyrotactic micro-organisms in a layer of finite depth. *Journal of Fluid Mechanics*, 208:509–543.

[Hillesdon and Pedley, 1996] Hillesdon, A. and Pedley, T. (1996). Bioconvection in suspensions of oxytactic bacteria: linear theory. *Journal of Fluid Mechanics*, 324:223–259.

[Hillesdon et al., 1995] Hillesdon, A., Pedley, T., and Kessler, J. (1995). The development of concentration gradients in a suspension of chemotactic bacteria. *Bulletin of mathematical biology*, 57:299–344.

[Hosoya et al., 2010] Hosoya, C., Akiyama, A., Kage, A., Baba, S. A., and Mogami, Y. (2010). Reverse bioconvection of chlamydomonas in the hyper-density medium. *Biological Sciences in Space*, 24(3_4):145–152.

[Jánosi et al., 2002] Jánosi, I. M., Czirók, A., Silhavy, D., and Holczinger, A. (2002). Is bioconvection enhancing bacterial growth in quiescent environments? *Environmental Microbiology*, 4(9):525–531.

[Jánosi et al., 1998] Jánosi, I. M., Kessler, J. O., and Horváth, V. K. (1998). Onset of bioconvection in suspensions of bacillus subtilis. *Physical Review E*, 58(4):4793.

[Kamiya and Witman, 1984] Kamiya, R. and Witman, G. B. (1984). Submicromolar levels of

calcium control the balance of beating between the two flagella in demembranated models of chlamydomonas. *The Journal of Cell Biology*, 98(1):97–107.

[Kessler, 1985] Kessler, J. O. (1985). Hydrodynamic focusing of motile algal cells. *Nature*, 313(5999):218–220.

[Kessler, 1986] Kessler, J. O. (1986). Individual and collective fluid dynamics of swimming cells. *Journal of Fluid Mechanics*, 173:191–205.

[Kok et al., 2016] Kok, V. J., Lim, M. K., and Chan, C. S. (2016). Crowd behavior analysis: A review where physics meets biology. *Neurocomputing*, 177:342–362.

[Lanza and Meloni, 2006] Lanza, R. and Meloni, A. (2006). *The Earth's Magnetic Field*. Springer.

[Lauga, 2011] Lauga, E. (2011). Life around the scallop theorem. *Soft Matter*, 7(7):3060–3065.

[Lauga and Powers, 2009] Lauga, E. and Powers, T. R. (2009). The hydrodynamics of swimming microorganisms. *Reports on progress in physics*, 72(9):096601.

[Lefèvre and Bazylinski, 2013] Lefèvre, C. T. and Bazylinski, D. A. (2013). Ecology, diversity, and evolution of magnetotactic bacteria. *Microbiology and Molecular Biology Reviews*, 77(3):497–526.

[López et al., 2015] López, H. M., Gachelin, J., Douarche, C., Auradou, H., and Clément, E. (2015). Turning bacteria suspensions into superfluids. *Physical review letters*, 115(2):028301.

[Lopez et al., 2012] Lopez, U., Gautrais, J., Couzin, I. D., and Theraulaz, G. (2012). From behavioural analyses to models of collective motion in fish schools. *Interface focus*, 2(6):693–707.

[Lukeman et al., 2010] Lukeman, R., Li, Y.-X., and Edelstein-Keshet, L. (2010). Inferring individual rules from collective behavior. *Proceedings of the National Academy of Sciences*, 107(28):12576–12580.

[Mathijssen, 2016] Mathijssen, A. (2016). *Hydrodynamics of micro-swimmers in complex fluids and environments*. PhD thesis, University of Oxford.

[Mlot et al., 2011] Mlot, N. J., Tovey, C. A., and Hu, D. L. (2011). Fire ants self-assemble into waterproof rafts to survive floods. *Proceedings of the National Academy of Sciences*, 108(19):7669–7673.

[Murat et al., 2015] Murat, D., Hérisse, M., Espinosa, L., Bossa, A., Alberto, F., and Wu, L.-F. (2015). Opposite and coordinated rotation of amphitrichous flagella governs oriented swimming and reversals in a magnetotactic spirillum. *Journal of bacteriology*, 197(20):3275–3282.

[Nadkarni et al., 2013] Nadkarni, R., Barkley, S., and Fradin, C. (2013). A comparison of

methods to measure the magnetic moment of magnetotactic bacteria through analysis of their trajectories in external magnetic fields. *PloS one*, 8(12):e82064.

[Nägeli, 1860] Nägeli, C. (1860). Ortsbewegungen der pflanzenzellen und ihrer theile (strömungen). *Beiträge zur wissenschaftlichen Botanik*, 2:59–108.

[Ng and Bassler, 2009] Ng, W.-L. and Bassler, B. L. (2009). Bacterial quorum-sensing network architectures. *Annual review of genetics*, 43:197–222.

[Pedley and Kessler, 1992] Pedley, T. and Kessler, J. (1992). Bioconvection. *Science Progress (1933-)*, pages 105–123.

[Pedley and Kessler, 1990] Pedley, T. and Kessler, J. O. (1990). A new continuum model for suspensions of gyrotactic micro-organisms. *Journal of fluid mechanics*, 212:155–182.

[Peng et al., 2021] Peng, Y., Liu, Z., and Cheng, X. (2021). Imaging the emergence of bacterial turbulence: Phase diagram and transition kinetics. *Science advances*, 7(17):eabd1240.

[Pierce et al., 2020] Pierce, C. J., Wijesinghe, H., Osborne, E., Mumper, E., Lower, B., Lower, S., and Sooryakumar, R. (2020). Tunable self-assembly of magnetotactic bacteria: Role of hydrodynamics and magnetism. *AIP Advances*, 10(1):015335.

[Platt, 1961] Platt, J. R. (1961). bioconvection patterns in cultures of free-swimming organisms. *Science*, 133(3466):1766–1767.

[Plesset and Winet, 1974] Plesset, M. S. and Winet, H. (1974). Bioconvection patterns in swimming microorganism cultures as an example of rayleigh-taylor instability. *Nature*, 248(5447):441–443.

[Popp et al., 2014] Popp, F., Armitage, J. P., and Schüler, D. (2014). Polarity of bacterial magnetotaxis is controlled by aerotaxis through a common sensory pathway. *Nature communications*, 5(1):1–9.

[Purcell, 1977] Purcell, E. M. (1977). Life at low reynolds number. *American journal of physics*, 45(1):3–11.

[Ramos et al., 2020] Ramos, G., Cordero, M. L., and Soto, R. (2020). Bacteria driving droplets. *Soft Matter*, 16(5):1359–1365.

[Rosenblatt et al., 1982] Rosenblatt, C., de Araujo, F. F. T., and Frankel, R. B. (1982). Birefringence determination of magnetic moments of magnetotactic bacteria. *Biophysical journal*, 40(1):83–85.

[Rosenblatt et al., 1985] Rosenblatt, C., Frankel, R. B., and Blakemore, R. P. (1985). A birefringence relaxation determination of rotational diffusion of magnetotactic bacteria. *Biophysical journal*, 47(3):323.

[Schaller et al., 2010] Schaller, V., Weber, C., Semmrich, C., Frey, E., and Bausch, A. R. (2010). Polar patterns of driven filaments. *Nature*, 467(7311):73–77.

[Schleifer et al., 1991] Schleifer, K. H., Schüler, D., Spring, S., Weizenegger, M., Amann, R.,

Ludwig, W., and Köhler, M. (1991). The genus magnetospirillum gen. nov. description of magnetospirillum gryphiswaldense sp. nov. and transfer of aquaspirillum magnetotacticum to magnetospirillum magnetotacticum comb. nov. *Systematic and applied microbiology*, 14(4):379–385.

[Schüler and Frankel, 1999] Schüler, D. and Frankel, R. B. (1999). Bacterial magnetosomes: microbiology, biomineralization and biotechnological applications. *Applied Microbiology and Biotechnology*, 52(4):464–473.

[Sumino et al., 2012] Sumino, Y., Nagai, K. H., Shitaka, Y., Tanaka, D., Yoshikawa, K., Chaté, H., and Oiwa, K. (2012). Large-scale vortex lattice emerging from collectively moving microtubules. *Nature*, 483(7390):448–452.

[Théry et al., 2020] Théry, A., Le Nagard, L., Ono-dit Biot, J.-C., Fradin, C., Dalnoki-Veress, K., and Lauga, E. (2020). Self-organisation and convection of confined magnetotactic bacteria. *Scientific reports*, 10(1):1–9.

[Trepat et al., 2009] Trepat, X., Wasserman, M. R., Angelini, T. E., Millet, E., Weitz, D. A., Butler, J. P., and Fredberg, J. J. (2009). Physical forces during collective cell migration. *Nature physics*, 5(6):426–430.

[Vicsek et al., 1995] Vicsek, T., Czirók, A., Ben-Jacob, E., Cohen, I., and Shochet, O. (1995). Novel type of phase transition in a system of self-driven particles. *Physical review letters*, 75(6):1226.

[Vicsek and Zafeiris, 2012] Vicsek, T. and Zafeiris, A. (2012). Collective motion. *Physics reports*, 517(3-4):71–140.

[Vincent and Hill, 1996] Vincent, R. and Hill, N. (1996). Bioconvection in a suspension of phototactic algae. *Journal of Fluid Mechanics*, 327:343–371.

[Wager, 1911] Wager, H. W. T. (1911). Vii. on the effect of gravity upon the movements and aggregation of euglena viridis, ehrb., and other micro-organisms. *Philosophical Transactions of the Royal Society of London. Series B, Containing Papers of a Biological Character*, 201(274-281):333–390.

[Wensink et al., 2012] Wensink, H. H., Dunkel, J., Heidenreich, S., Drescher, K., Goldstein, R. E., Löwen, H., and Yeomans, J. M. (2012). Meso-scale turbulence in living fluids. *Proceedings of the national academy of sciences*, 109(36):14308–14313.

[Wioland et al., 2013] Wioland, H., Woodhouse, F. G., Dunkel, J., Kessler, J. O., and Goldstein, R. E. (2013). Confinement stabilizes a bacterial suspension into a spiral vortex. *Physical review letters*, 110(26):268102.

[Witman, 1993] Witman, G. B. (1993). Chlamydomonas phototaxis. *Trends in cell biology*, 3(11):403–408.

[Yanaoka et al., 2009] Yanaoka, H., Inamura, T., and Suzuki, K. (2009). Numerical analysis of bioconvection generated by chemotactic bacteria. *Journal of Fluid Science and Techno-*

*logy*, 4(3):536–545.

[Yanaoka and Nishimura, 2022] Yanaoka, H. and Nishimura, T. (2022). Pattern wavelengths and transport characteristics in three-dimensional bioconvection generated by chemotactic bacteria. *Journal of Fluid Mechanics*, 952:A13.

[Zahn et al., 2017] Zahn, C., Keller, S., Toro-Nahuelpan, M., Dorscht, P., Gross, W., Laumann, M., Gekle, S., Zimmermann, W., Schüler, D., and Kress, H. (2017). Measurement of the magnetic moment of single magnetospirillum gryphiswaldense cells by magnetic tweezers. *Scientific Reports*, 7(1):1–14.

[Zhang et al., 2010] Zhang, H.-P., Be'er, A., Florin, E.-L., and Swinney, H. L. (2010). Collective motion and density fluctuations in bacterial colonies. *Proceedings of the National Academy of Sciences*, 107(31):13626–13630.